Applied Thermal Engineering 275 (2025) 126868

Contents lists available at ScienceDirect

Applied Thermal Engineering

journal homepage: www.elsevier.com/locate/apthermeng

Research Paper

Optimization design method for serpentine cold plates combining structural parameter tuning and topology optimization

Sen Zhan [a,b,*], Xingyu Zhao [a], Shuen Zhao [a], Shaojiang Dong [a], Yanli Yin [a]

[a] School of Mechatronics and Vehicle Engineering, Chongqing Jiaotong University, Chongqing 400074, China
[b] State Key Laboratory of Mechanical Transmission for Advanced Equipment, Chongqing University, Chongqing 400044, China

ARTICLE INFO

Keywords:
Lithium-ion battery
Battery thermal management system
Cold plate
Topology optimization

ABSTRACT

Lithium-ion batteries are the predominant power source for electric vehicle (EV), and their operational safety necessitates the implementation of advanced battery thermal management systems (BTMS) to mitigate risks such as thermal runaway. In engineering applications, serpentine cold plate (SCP) is widely employed as essential heat dissipation components within BTMS due to their structural simplicity and reliable thermal performance. However, conventional SCP often exhibit high pressure drops, resulting in substantial pump power consumption that constrains overall system efficiency. Traditional cold plate optimization methods primarily rely on adjusting geometric parameters, combined with optimization algorithms to improve the plate design. Although these approaches can enhance performance, they offer limited design freedom and are prone to falling into local optima. To overcome these limitations, this study presents a novel SCP design methodology that integrates traditional parametric optimization with topology optimization, thereby enhancing design flexibility and enabling the development of a new SCP configuration with improved comprehensive performance. The proposed approach maintains the inherent thermal advantages of serpentine flow structures while significantly reducing pressure drop and pump power consumption. Specifically, an orthogonal experimental design is conducted based on three key design variables—channel number, channel width, and channel height—and the second-generation non-dominated sorting genetic algorithm (NSGA-II) is employed to derive an optimized SCP configuration, referred to as OSCP. This optimized design is then used as the initial geometry for subsequent topology optimization, with objectives of maximizing heat transfer and minimizing flow dissipation, resulting in a topology-optimized SCP (TSCP). For performance benchmarking, a rounded SCP (RSCP) and a directly topology-optimized channel structure (TCP) are also introduced. Numerical simulation results reveal that the proposed hybrid optimization strategy yields substantial performance gains. Compared to OSCP, TSCP reduces pump power consumption (P_{pump}) by 49.3 % and enhances the comprehensive j/f performance index by 69.76 %. Furthermore, this method offers greater design freedom than traditional techniques, while avoiding the excessive structural complexity often associated with direct topology optimization, thereby improving convergence efficiency and manufacturability. These findings suggest that the proposed design approach provides an effective and practical pathway for the development of high-performance SCPs in advanced thermal management applications.

1. Introduction

With the increasingly severe global energy crisis and environmental pollution issues, EV has become an important direction for the transformation and upgrading of the automotive industry due to their low emissions and high efficiency. As the core component of EV, the power battery plays a crucial role in vehicle safety [1]. Lithium-ion batteries, widely used in EV due to their high energy density, long cycle life, and high efficiency, rely heavily on their operating temperature for performance. The optimal operating temperature range is between 15 °C and 40 °C [2]. When the temperature exceeds a certain threshold, the battery's performance and lifespan significantly degrade, and in extreme cases, it can lead to fires, explosions, and other hazards. Therefore, an efficient thermal management system is required to regulate the battery's operating temperature [3].

The main cooling methods in BTMS include air cooling [4,5], liquid cooling [6,7], phase change material (PCM) cooling [8,9], and heat pipe

* Corresponding author.
E-mail address: fishjason@163.com (S. Zhan).

https://doi.org/10.1016/j.applthermaleng.2025.126868
Received 24 February 2025; Received in revised form 30 April 2025; Accepted 16 May 2025
Available online 19 May 2025

Nomenclature

A_c	heat surface area (m^2)
$A_{f,w}$	wetted surface area (m^2)
c	specific heat capacity ($J{\cdot}kg^{-1}{\cdot}K^{-1}$)
D_a	Darcy number
D_h	hydraulic diameter (m)
d	width of the channels (mm)
F	body force (N)
f	flow resistance
h	height of the channel (mm)
h_c	heat transfer coefficient($W{\cdot}m^{-1}{\cdot}K^{-1}$)
J_1	objective function for heat exchange
J_2	objective function for dissipative power
j/f	comprehensive evaluation factor
k	thermal conductivity ($W{\cdot}m^{-1}{\cdot}K^{-1}$)
L	Characteristic length (m)
L_1	channel equivalent length (m)
n	Channel number
Nu	Nusselt number
Pr	Prandtl number
ΔP	pressure drop (Pa)
P_{pump}	pumping power (W)
Q_m	mass flow rate ($g{\cdot}s^{-1}$)
Q	heat generation (W)
q	penalty factor
Re	Reynolds number
R^2	Regression coefficients
T	temperature (°C)
u	velocity ($m{\cdot}s^{-1}$)
V_f	Volume fraction
W	heat flux ($W{\cdot}m^{-2}$)

Greek symbols

α	inverse permeability
β	projection slope
γ	design variable
γ_β	projection point
μ	dynamic viscosity ($kg{\cdot}m^{-1}{\cdot}s^{-1}$)
ρ	density ($kg{\cdot}m^{-3}$)
Ω	design domain
Φ	optimization objective
∇	gradient operator

Subscripts

avg	average
f	fluid
in	inlet
max	maximum
out	outlet
w	wet

Superscripts

*	dimensionless

Acronyms

2D	two-dimensional
3D	three-dimensional
BTMS	Battery thermal management system
CFD	Computational fluid dynamics
CNC	Computer numerical control
NSGA-II	Non-dominated sorting genetic algorithm-II
OSCP	Optimized serpentine cold plate
PCM	Phase change material
RSCP	Rounded serpentine cold plate
SCP	Serpentine cold plate
TSCP	Topology-optimized serpentine cold plate
TCP	Topology-optimized cold plate

cooling [10,11]. Air cooling is cost-effective and simple in structure, but its heat transfer efficiency is limited, making it unsuitable for high-power applications. PCM cooling absorbs heat through phase change but has slow response times and limited thermal capacity. Heat pipe cooling offers high thermal conductivity but is complex to design, manufacture, and maintain. Liquid cooling, due to its high heat transfer efficiency, cooling capacity, and compact structure, has become the mainstream solution for EV battery thermal management and is widely used in the market [12].

In the research on liquid cooling, the focus is mainly on the design and analysis of cold plate structures, which can generally be categorized into three types: traditional structures, biomimetic structures, and topology-optimized structures. Traditional structures refer to those based on engineering experience with simple and regular flow channel layouts, such as parallel, serpentine, U-shaped channels, and others [13–15]. Monika et al. [16] explored the impact of channel layout and inlet position in parallel-flow cold plates, emphasizing that placing the inlet near the battery tab region and adopting an appropriate number of channels can achieve a good balance between thermal uniformity and pressure drop under given conditions. Mubashir et al. [17] designed a double serpentine channel cold plate to improve the thermal performance of single serpentine channel cold plates under various operating conditions. Patil et al. [18] studied multi-channel U-shaped plates and found that a cold plate with alternating inlet and outlet distributions reduced the maximum temperature T_{max} by 32.2 % compared to a single inlet–outlet configuration. Qi et al. [19] and others designed a multi-U-shaped microchannel cold plate, which reduced T_{max} by 5.83 K and ΔP by 89 %. Biomimetic structures are often inspired by biological structures or natural phenomena, such as leaf vein structures, honeycomb structures, tree-like structures and others [20–22]. Zhan et al. [23] used a biomimetic leaf vein structure as an initial solution for topology optimization, resulting in a biomimetic leaf vein topology cold plate, which showed a 96 % improvement in overall performance compared to the initial cold plate. Yan et al. [24] extracted a biomimetic leaf vein structure based on leaf vein contours, and their design reduced T_{max} by 10.17 K and improved heat transfer efficiency by 22.43 % compared to a rectangular cold plate. Zhang et al. [25] optimized the design of traditional straight-channel rectangular fin plates, and then biomimetically designed the fins based on horseshoe-shaped fins, resulting in better thermal performance. Wang et al. [26] designed a novel butterfly-shaped channel structure and optimized it using an objective function, which achieved better cooling performance and temperature uniformity with the outlet positioned between the positive and negative electrodes. Topology-optimized structures optimize material distribution based on topology optimization algorithms, guided by objective functions. This approach has shown great potential in cold plate structure optimization. Recent studies have increasingly focused on multi-objective topology optimization, topology optimization under non-uniform heat load conditions, and biomimetic topology optimization [27–29]. Pandey et al. [30] used ΔP and T_{avg} as objective functions and constraints to generate free-form and non-intuitive fin structures based on topology optimization methods. Under the same P_{pump}, the drop-oblique-trapezoidal and oval-shaped fins demonstrated a reduction in T_{avg} by 3 to 6 °C compared to the size-optimized biased strip fins and stepped fins. Wu et al. [31]

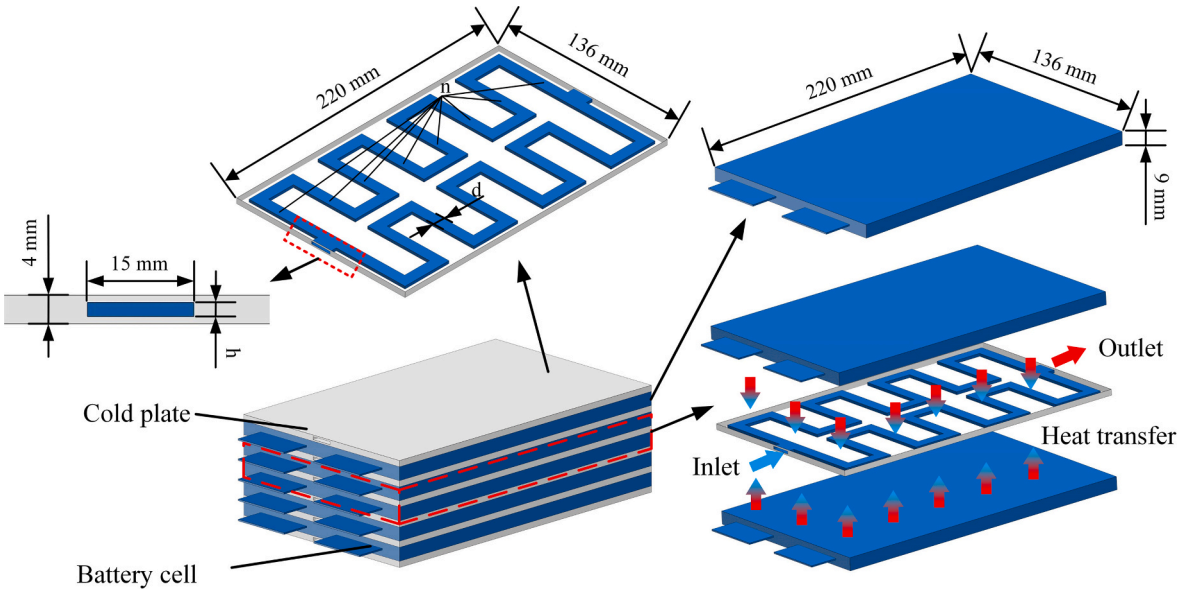

Fig. 1. Structural model of the cold plate and battery pack.

applied topology optimization methods based on non-uniform heat sources to design a novel topology-optimized cold plate. Under the same mass flow rate, the maximum heat transfer coefficient of the optimized plate was increased by 26 % compared to conventional plates, and the maximum temperature deviation was reduced by 20 %. Wang et al. [32] performed multi-objective topology optimization to balance ΔP and temperature, designing both laminar and turbulent cold plates. Under high turbulent flow conditions, the turbulent cold plate exhibited better cooling performance than laminar, serpentine, and rectangular cold plates, with the PEC increased by 86.7 %. Among various structures, although biomimetic structures are inspired by nature to design efficient fluid flow and heat transfer structures, and topology-optimized structures generate the best layout through optimization algorithms to enhance cooling efficiency, traditional structures are the most commonly used in engineering applications due to their simpler design and manufacturing processes.

SCP, known for their excellent heat dissipation efficiency, reliability, and simple structure, are widely used in liquid cooling systems for power batteries. The traditional design methods for these cold plates can be divided into two main approaches: one based on mathematical models of fluid dynamics and thermal characteristics, and the other based on simulation data combined with optimization algorithms. For the first approach, Cho et al. [33] studied the fluid dynamics behavior and thermal performance of novel vascular channels with semi-circular cross-sections using a numerical analytical model. E et al. [34] developed thermal resistance models for SCP, along with pressure loss models for straight pipe and U-shaped pipe configurations. Through mathematical modeling, they determined the optimal parameter structure. However, mathematical modeling methods are often limited by the difficulty in translating physical phenomena into mathematical models and the complexity of the calculations, leading to their limited application. For the second approach, Guo et al. [35] compared four types of serpentine structures and found that the spiral serpentine channel exhibited the best overall performance. Orthogonal testing was then conducted on multiple parameters to optimize the structural parameters and flow rate through range and variance analysis. Zhang et al. [36] proposed a new type of symmetric, complex serpentine channel cold plate and introduced Y-shaped fins. Orthogonal experiments were conducted on the fin design to further improve the thermal performance of the liquid cooling plate. Jiang et al. [37] used Bayesian multi-objective optimization to optimize the width, depth, and bending radius of serpentine channels. Compared to the initial design, the optimized design showed a slight decrease in maximum temperature T_{max}, while the pump power consumption was reduced by 71 %. Shrinet et al. [38] introduced thermal conductive elements between the battery and coolant channels, designed an orthogonal test, and used NSGA-II for optimization, improving temperature uniformity by 71.7 %. However, traditional optimization methods are constrained by predefined design conditions, which limit both design flexibility and search efficiency. Consequently, they are susceptible to local optima and offer limited improvements in pressure drop and energy consumption control, preventing full exploitation of the performance potential of the SCP.

To address the challenges of excessive pressure drop and high power consumption commonly associated with SCP, this study introduces a novel channel design methodology that synergistically combines traditional optimization techniques with topology optimization. By capitalizing on the high design flexibility inherent in topology optimization, the proposed approach aims to unlock the full thermal–hydraulic performance potential of SCP. The method begins with an orthogonal experimental design to identify key geometrical parameters, followed by parametric optimization using an evolutionary algorithm to obtain a baseline optimized SCP configuration. This configuration subsequently serves as the initial design input for topology optimization of the internal flow channel, with objectives of minimizing flow resistance and maximizing heat transfer. Comprehensive numerical evaluations demonstrate that TSCP achieves substantial reductions in both pressure drop and pump power consumption while enhancing overall performance, thereby validating the efficacy of the proposed hybrid design strategy.

2. Model description

The layout of EV batteries greatly influences their heat dissipation efficiency and safety. Fig. 1 shows the layout of the battery and cold plate, as well as the structure of the cooling plate. The battery and cooling plate are stacked alternately, allowing the coolant to be distributed more evenly around the battery, effectively dissipating the heat generated during battery discharge. The cold plate studied in this paper consists of symmetric serpentine channels, with the area of the cooling plate equal to the area of the battery. The cold plate measures 220 mm in length, 136 mm in width, and 4 mm in height. The inlet and outlet channel widths are fixed at 15 mm, with the height of the channel denoted as h, the internal width of the channel as d, and the number of channels as n.

3. Optimization design of SCP

3.1. Governing equations

(1) The mass conservation equation (continuity equation) expanded term by term in Cartesian coordinates [39]:

$$\frac{\partial \rho_f}{\partial t}+\frac{\partial \rho_f u_x}{\partial x}+\frac{\partial \rho_f u_y}{\partial y}+\frac{\partial \rho_f u_z}{\partial z}=0 \tag{1}$$

where ρ_f is the fluid density, with water being the fluid in this study, and u_x, u_y, u_z are the velocity components of the flow velocity u in the x ,y, and z directions, respectively. The equation is compressed and simplified using the gradient operator:

$$\frac{\partial \rho_f}{\partial t}+\nabla(\rho_f \vec{u})=0 \tag{2}$$

(2) Momentum Equation [39]:

$$\frac{\partial \rho_f}{\partial t}\vec{u}+\nabla\cdot(\rho_f \vec{u})\vec{u}=\nabla P \tag{3}$$

where $\vec{u}$ is the velocity vector, and P is the pressure.

(3) Energy equation [39]:

$$\rho_f c\frac{\partial T_f}{\partial t}+\nabla\cdot(\rho_f c\vec{u}T_f)=\nabla\cdot(\lambda_f \nabla T_f) \tag{4}$$

where $\vec{u}$ is the velocity vector, c is the specific heat capacity of the fluid, T_f is the temperature of the fluid, and λ_f is the thermal conductivity of the fluid.

3.2. Parameter definitions

The Reynolds number (Re) is used to evaluate the flow regime of the fluid, determining whether it is laminar or turbulent. The formula for calculating the Reynolds number within the cold plate is as follows [40]:

$$Re=\frac{\rho_f u_{in} D_h}{\mu} \tag{5}$$

where u_{in} is the fluid velocity at the inlet, D_h is the hydraulic diameter of the channel, and μ is the dynamic viscosity.

The hydraulic diameter is calculated as follows [41]:

$$D_h=\frac{4V_w}{A_{f,w}} \tag{6}$$

where V_w is the volume of the liquid domain, and $A_{f,w}$ is the wetted surface area of the liquid domain.

In the initial numerical simulation, T_{max} refers to the highest temperature point in the working area, which directly relates to the thermal safety and performance stability of the device. T_{avg} is used to evaluate the overall thermal distribution uniformity of the cold plate [42].

$$T_{\text{avg}}=\frac{\int_{A_c} T dA_c}{\int_{A_c} dA_c} \tag{7}$$

where A_c is the heat transfer surface area of the cold plate.

In the heat dissipation process of the cold plate, the fluid flow needs to be driven by a pump. Therefore, to evaluate the power consumption required by the pump to drive the coolant in the BTMS, it is intuitively represented in the form of ΔP.

$$\Delta P=P_{in}-P_{out} \tag{8}$$

Table 1
Cold plate and coolant physical parameters.

Properties	c ($J\cdot kg^{-1}\cdot K^{-1}$)	k ($W\cdot m^{-1}\cdot k^{-1}$)	ρ ($kg\cdot m^{-3}$)	μ (Pa·s)
Cold plate (Aluminum)	903	237	2702	–
Coolant (Water)	4181.72	0.62	997.561	1.003E-3

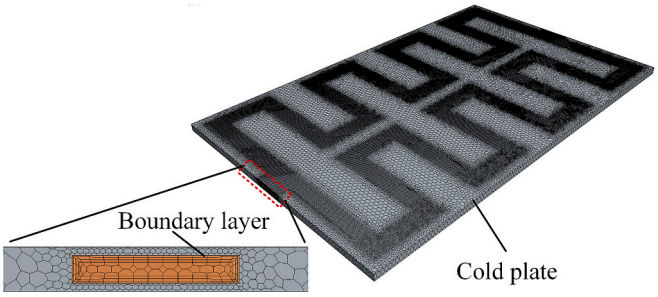

Fig. 2. Mesh model of the cold plate.

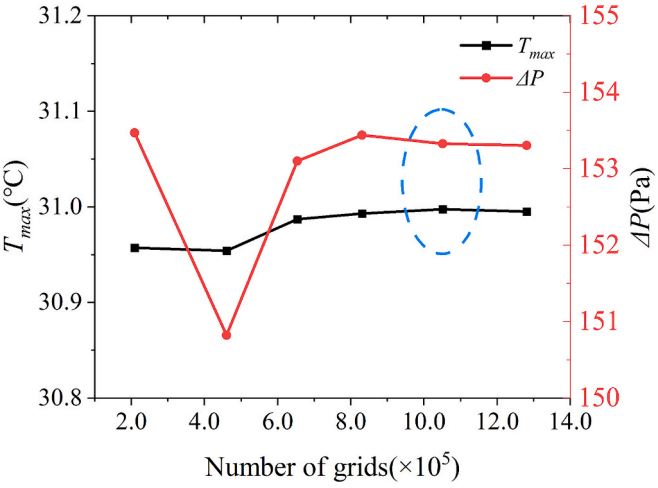

Fig. 3. Mesh Independence Verification.

where P_{in} is the pressure at the inlet, and P_{out} is the pressure at the outlet. Table 1 lists the main physical parameters of the cold plate and coolant used in the simulation.

3.3. Boundary conditions

The actual heat dissipation process of the cooling plate is affected by various factors, such as the environment and the material of the cooling plate. To ensure the feasibility of the numerical simulation, the following assumptions are made:

(1) The aluminum cooling plate material is homogeneous and isotropic.
(2) The coolant is assumed to be in a laminar flow state and treated as an incompressible fluid.
(3) The inlet is a mass flow inlet, with an inlet temperature of 25 °C and a mass flow rate of 2 g/s.
(4) The outlet is set as a pressure outlet, with a static temperature of 25 °C and a pressure of 0 Pa.
(5) The upper and lower surfaces of the cooling plate are treated as heat transfer walls, with heat flux calculated based on the 3C

Table 2
Main performance parameters of battery.

Parameter	Value
Battery capacity (Ah)	30
Nominal voltage (V)	3.7
Length, Width, Height (mm)	220 × 136 × 9
Internal resistance (mΩ)	2
Density (kg/m^3)	2042.48
Maximum charging voltage (V)	4.2 ± 0.05
Discharge cut-off voltage (V)	2.75

discharge of a single battery. The remaining four surfaces are set as adiabatic walls.

3.4. Mesh independence verification

To ensure the accuracy and reliability of the numerical simulation in finite element analysis, a mesh independence verification is required. This involves observing how the numerical simulation results change with varying mesh densities to determine whether the results stabilize at a certain mesh level. In this study, the geometric model was meshed in STAR CCM+, using a polyhedral-prism layer mesh generator. The mesh model is shown in Fig. 2. Fig. 3 presents the variation of the maximum temperature and ΔP of the cold plate simulation model with increasing mesh density. It was found that no significant changes occurred after the mesh count exceeded 1,051,214. Considering both accuracy and computational efficiency, a mesh density of 1,051,214 was chosen for the numerical simulation.

3.5. Experimental setup

3.5.1. Battery temperature rise test

This study investigates a 30 Ah pouch lithium-ion battery, with its detailed parameters provided in Table 2. The temperature rise data of the battery was obtained from charge-discharge temperature rise experiments conducted using the test platform shown in Fig. 4(b) Four thermocouples were positioned at four locations on the battery's surface, and the battery was insulated with thermal insulation cotton. It was then placed in a constant temperature and humidity chamber set to 25 °C, ensuring an adiabatic environment. The temperature rise data was measured at charge–discharge rates ranging from 0.5C to 1.5C. The battery heat generation model is established based on the classical Bernardi equation [43]:

$$Q = I\left(U_{OCV} - U + T\frac{\partial U_{OCV}}{\partial T}\right) \tag{9}$$

where Q is the heat generation rate, U is the operating voltage, U_{OCV} is the open-circuit voltage, and I is the operating current. The term $I(U_{OCV} - U)$ corresponds to the Joule heat generated by the internal resistance R_j of the battery, while $IT(\partial U_{OCV}/\partial T)$ represents the heat generated by internal electrochemical reactions. Thus, the total heat generation can be expressed as:

$$Q = I^2R_j + IT\frac{\partial U_{OCV}}{\partial T} \tag{10}$$

The heat absorption of the battery can be expressed as:

$$Q^* = mc_p\frac{dT}{dt} \tag{11}$$

where m is the battery mass, and c_p is the specific heat capacity of the battery. In an adiabatic environment, Q and Q^* are equal, thus we can obtain:

$$\frac{dT}{dt} = I^2\frac{R_j}{mc_p} + I\frac{T}{mc_p}\frac{\partial U_{OCV}}{\partial T} \tag{12}$$

The relationship between the rate of temperature change dT/dt and the current I is obtained by fitting the experimental battery data as follows:

$$\frac{dT}{dt} = 4.379 \times 10^{-6}I^2 + 1.468 \times 10^{-4}I \tag{13}$$

By combining with Equation (11), the heat generation relationship can be expressed as:

$$Q = mc_p\left(\frac{dT}{dt}\right) = 2 \times 10^{-3}I^2 + 0.067I \tag{14}$$

The expression for the heat generation rate per unit volume (q) of the battery is as follows:

$$q = \frac{Q}{V} = 7.43I^2 + 248.99I \tag{15}$$

where V is the cell volume. The heat flux (W) calculation formula is:

$$W = q \cdot h \tag{16}$$

Based on the fitted equation, the specific heat capacity of a single battery is calculated to be 830.41 J/(kg·K). To save computational resources, the actual non-uniform battery thermal model is simplified to a uniform model. The accuracy of this simplified model is verified by comparing the experimental and simulation data shown in Fig. 5. In the simplified model, the surface heat flux is considered as the product of the heat generation per unit volume and the battery thickness. The heat flux

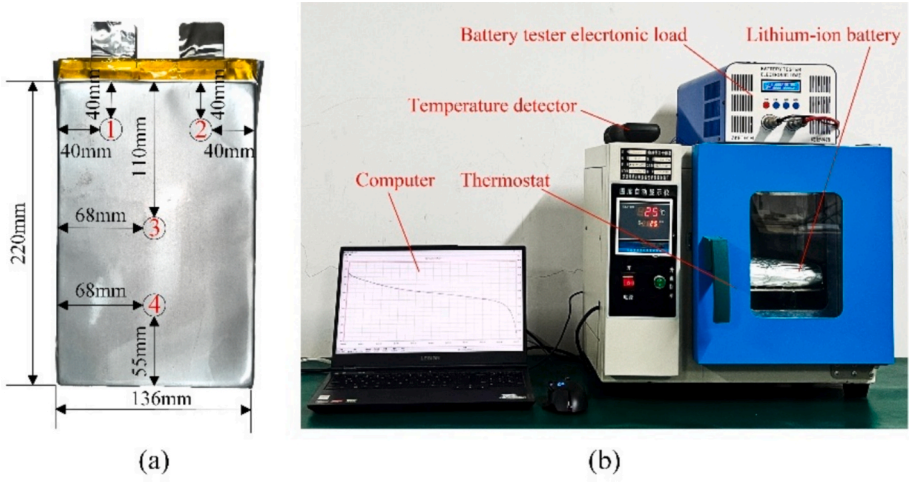

Fig. 4. Battery experiment: (a) Lithium-ion battery; (b) battery experimental apparatus.

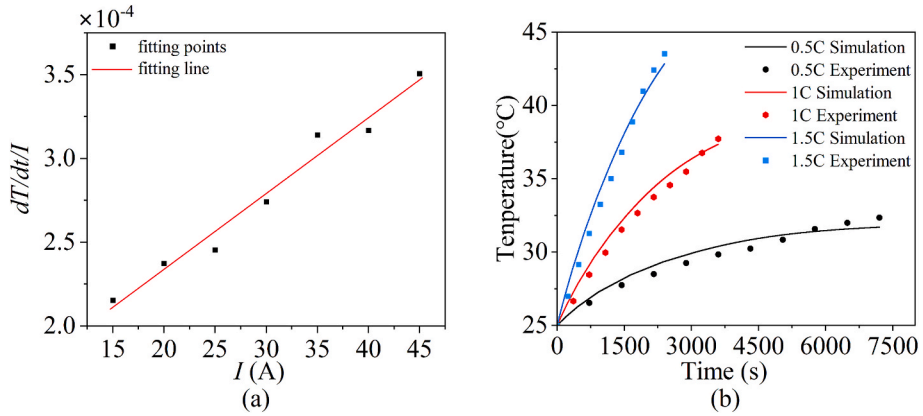

Fig. 5. (a) Fitting of experimental data; (b) Comparison between the battery model simulation and experimental data.

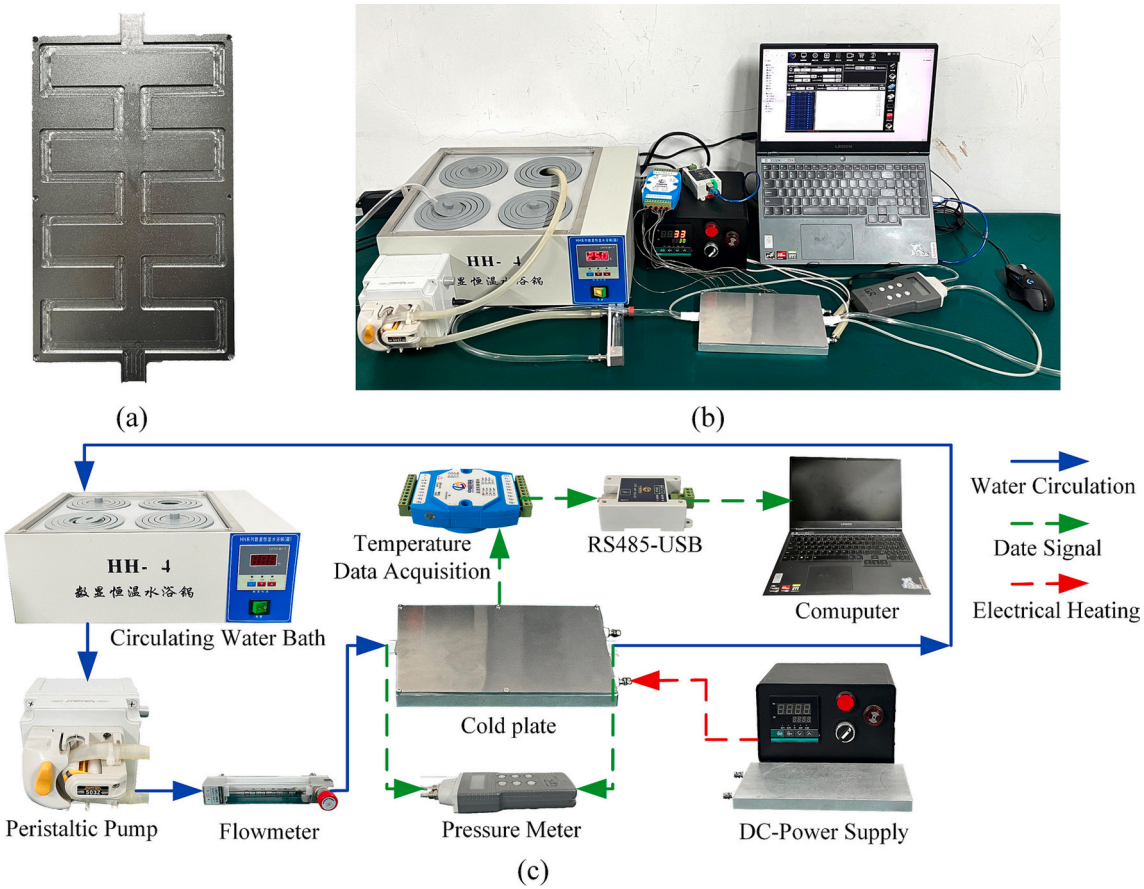

Fig. 6. Cold plate heat dissipation experiment: (a) Cold plate; (b) cooling experimental platform; (c) connection diagram of the experimental devices.

at a 3C discharge rate is calculated to be 743.33 W/m^2.

3.5.2. *Cold plate heat dissipation experiment*

To verify the accuracy and reliability of the simulation, this study designed an experimental investigation of the heat transfer performance of the cold plate under mass flow rates ranging from 1 to 5 g/s. The cold plate, consisting of an aluminum base and cover plate, was manufactured using a CNC machine, as shown in Fig. 6. The plates were secured with screws and sealed with adhesive. The experiment comprised three main systems: the liquid flow system, the heating system, and the data acquisition system. The specific instruments used are listed in Table 3. In the liquid flow system, a thermostatic water bath maintained a constant coolant temperature, while a peristaltic pump ensured a stable liquid

Table 3
Experimental equipment, usage range, and accuracy.

Equipment	Usage Range	Accuracy
Rotor flowmeter	25 ~ 400 ml/min	±2.5 %
Peristaltic pump	20 ~ 555 ml/min	±5 %
Thermostatic water bath	5 ~ 100 °C	±0.5 %
Temperature acquisition module	−40 ~ 85 °C	±0.25
Digital pressure gauge	0 ~ ±30 psi	±0.2 %
Aluminum block	0 ~ 400 °C	±0.15 %
DC power	0 ~ 100 V; 0 ~ 3 A	0.1 %+5 mV; 0.1 %+10 mA

Table 4
Cooling plate experimental and simulation data.

	Q_m (g/s)	1	2	3	4	5
T_{avg} (℃)	Simulation	32.74	29.09	27.82	27.19	26.82
	Experimental	33.9	30.1	28.8	28.1	27.6
	error	3.54 %	3.47 %	3.52 %	3.35 %	2.91 %
ΔP (Pa)	Simulation	64.07	153.32	272.79	422.96	602.8
	Experimental	68.2	163.5	291.2	437.9	625.4
	error	6.45 %	6.64 %	6.75 %	3.53 %	3.75 %

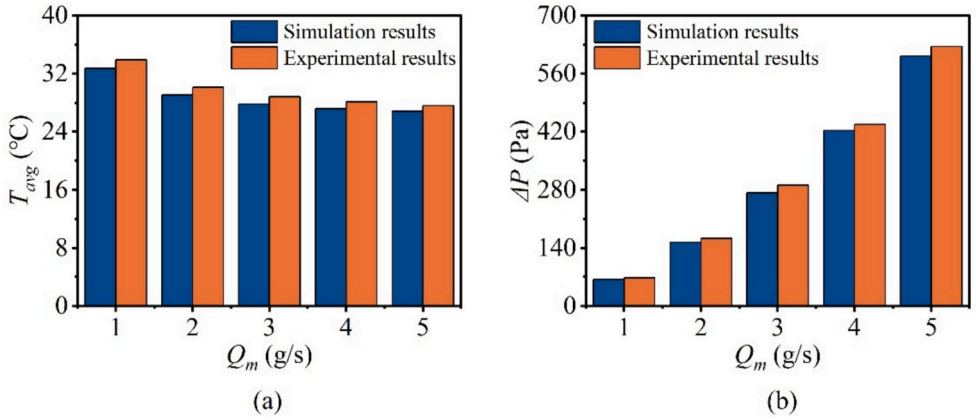

Fig. 7. Comparison of simulation and experimental results: (a) T_{avg}; (b) ΔP.

flow rate. A rotor flowmeter measured and recorded the flow rate in real time, ensuring the stability of experimental conditions and the accuracy of data. In the data acquisition system, a temperature acquisition module monitored temperature variations of the cold plate in real time and transmitted the data to a computer. A digital pressure gauge displayed the ΔP between the inlet and outlet, providing reliable data for evaluating fluid performance. The heating system used a DC power source to drive heating rods, providing a stable heat source. Aluminum blocks replaced batteries to distribute heat uniformly, ensuring both experimental safety and uniform heat distribution.

3.5.3. Experimental results and analysis

By analyzing the data in Table 4, it can be concluded that for mass flow rates ranging from 1 g/s to 5 g/s, the maximum error between the simulation and experimental results for the T_{avg} does not exceed 3.54 %, while the maximum error for the ΔP is 6.75 %. From the comparison shown in Fig. 7, it is evident that the trends of both the simulation and experimental results align closely, demonstrating good consistency and validating the reliability of the simulation model in this study.

3.6. Orthogonal experimental design and results

3.6.1. Orthogonal experimental design

When conducting multi-factor and multi-level experiments, a comprehensive trial can require a vast number of experiments, significantly increasing the time and cost. However, orthogonal testing can effectively avoid this issue. The orthogonal experimental design allows for the selection of representative data combinations from multiple factors and levels for analysis, thus avoiding repetitive trials, reducing computational resource consumption, and ensuring the accuracy of the entire experiment. In this study, a three-factor, four-level orthogonal experiment was designed with three variables: number of channels (n), channel width (d), and channel height (h). The experimental design is shown in Table 5, with the results of the 16 orthogonal experiments represented by T_{max}, T_{avg}, and ΔP, as shown in Table 6.

Table 5
Orthogonal experiment factor levels.

FactorLevel	n	d (mm)	h (mm)
1	6	7	1.5
2	8	8	2
3	10	9	2.5
4	12	10	3

As shown in Fig. 8, the temperature cloud maps of the cross-sections of the cold plates in the 16 orthogonal test groups are displayed. By observing the results, it is evident that the heat distribution is relatively uniform in all cases. The temperature gradually increases from the inlet to the outlet, with the symmetrically distributed channels ensuring an even heat distribution. The high-temperature zones are mainly concentrated near the outlet of the cold plate. However, the highest

Table 6
Orthogonal experiment scheme and results.

Test group	Factor			Evaluation index		
	n	d (mm)	h (mm)	T_{max} (℃)	T_{avg} (℃)	ΔP (Pa)
1	1	1	1	31.18	29.31	329.22
2	1	2	2	31.27	29.38	127.88
3	1	3	3	31.41	29.49	61.44
4	1	4	4	31.59	29.61	32.91
5	2	1	2	30.91	29.03	191.19
6	2	2	1	30.90	28.96	318.52
7	2	3	4	31.18	29.23	47.34
8	2	4	3	31.14	29.20	61.22
9	3	1	3	30.91	28.90	136.00
10	3	2	4	31.02	28.96	68.49
11	3	3	1	30.81	28.78	305.40
12	3	4	2	30.89	28.87	121.08
13	4	1	4	30.94	28.81	99.85
14	4	2	3	30.89	28.78	119.63
15	4	3	2	30.82	28.75	162.95
16	4	4	1	30.75	28.66	292.46

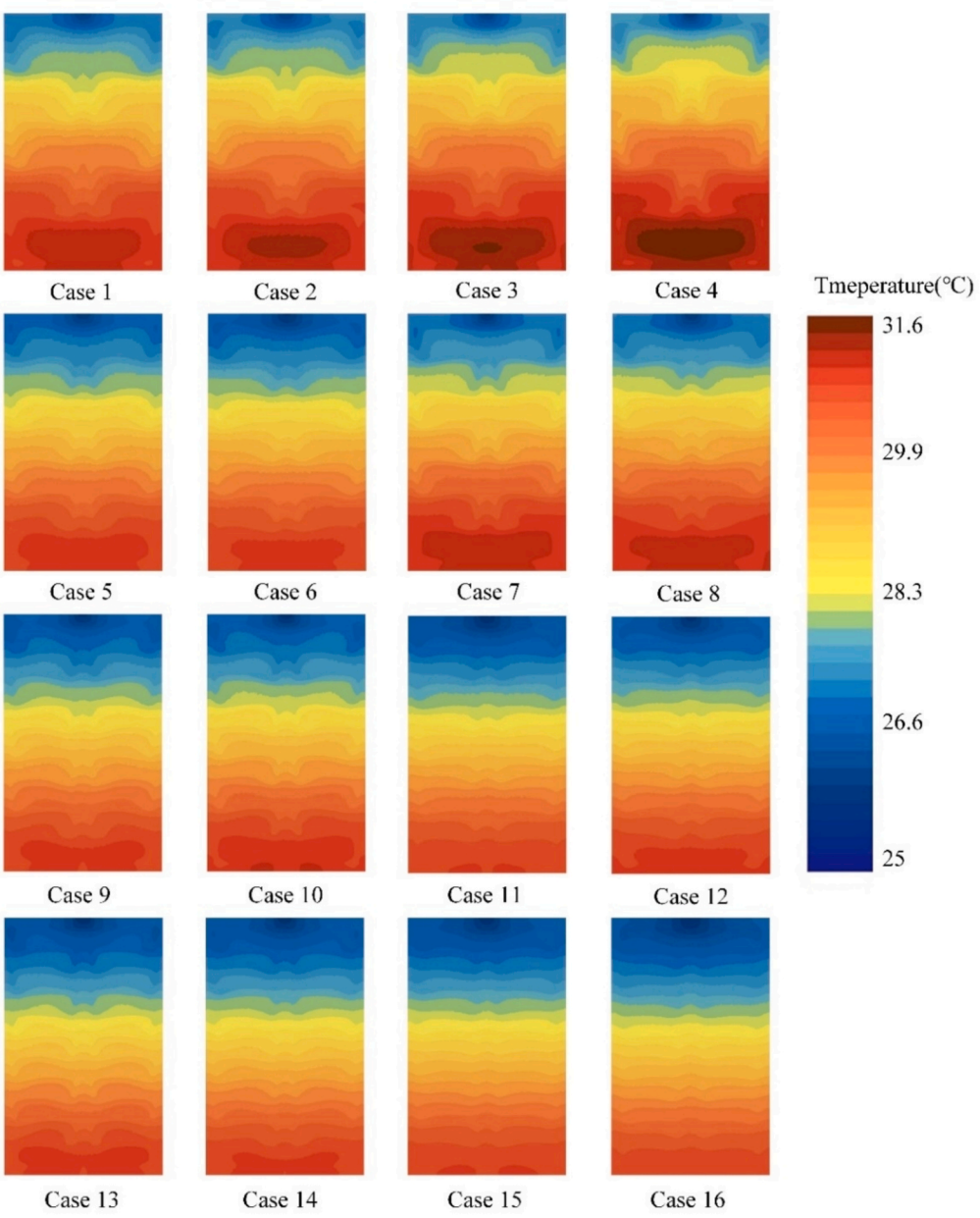

Fig. 8. Orthogonal test temperature cloud map.

temperature in all cases does not exceed 31.6 °C, effectively keeping the battery at a lower temperature. This is beneficial for enhancing the thermal stability and safety of the battery, demonstrating the superiority of this cold plate design in terms of efficient heat dissipation and uniformity control.

3.6.2. Analysis of orthogonal test results

Range analysis is a method used to evaluate the impact of each factor on the results in an experiment. The larger the value of the range (R), the greater the influence of the factor [44]. Range analysis is performed on the 16 sets of data from the orthogonal test to determine a relatively optimal parameter combination. The results are shown in Table 7, where the average value of each factor level is denoted as k_i. The calculation of R is shown in formula (10):

$$R = \{\max\{k_1, k_2, k_3\} - \min\{k_1, k_2, k_3\}\} \tag{17}$$

According to the range analysis data in Table 7, under the T_{max} indicator, the highest temperature point in the working area is shown. The influence of the three factors is ranked as $n > h > d$, with n being the most significant factor. The more flow channels there are, the lower the T_{max}, and the higher the thermal safety. Under the T_{avg} indicator, the overall thermal distribution uniformity is shown. The influence of the three factors is ranked as $n > h > d$, with n being the most significant factor. The more flow channels there are, the lower the T_{avg}, and the more uniform the heat distribution. Under the ΔP evaluation index, the degree of influence of each structural factor on pump power consumption is shown. The influence of the three factors is ranked as $h > d > n$, with flow channel height being the most significant factor. The lower the flow channel height, the higher the ΔP, and the greater the pump power consumption.

3.7. Optimization design based on NSGA-II

The NSGA-II is a multi-objective optimization algorithm designed to improve computational efficiency. By introducing crowding distance and elite retention strategies, it enhances global search capabilities and

Table 7
Range analysis results.

	k_i	n	d	h
T_{max}/(℃)	k_1	31.36	30.98	30.91
	k_2	31.03	31.02	30.97
	k_3	30.91	31.06	31.09
	k_4	30.85	31.09	31.18
	R	0.51	0.11	0.27
T_{avg}/(℃)	k_1	29.45	29.01	28.93
	k_2	29.11	29.02	29.01
	k_3	28.88	29.06	29.09
	k_4	28.75	29.09	29.15
	R	0.70	0.08	0.22
ΔP/(Pa)	k_1	137.86	189.07	311.40
	k_2	154.57	158.63	150.78
	k_3	157.74	144.28	94.57
	k_4	168.73	126.92	62.15
	R	30.86	62.15	249.25

the quality of solutions [45]. In multi-objective design, to reduce computational load, this study uses the least squares method to establish surrogate models, fitting the objective functions using 16 sets of orthogonal experimental data, in order to achieve fast and accurate optimization. With T_{max}, T_{avg}, and ΔP as the objective functions, where x_1, x_2, and x_3 represent the number of channels n, channel width d, and channel height h respectively, the data obtained from the orthogonal experiments is fitted, resulting in the following predictive models:

$$\begin{aligned} &T_{max}(n,d,h) = F_1(x_1,x_2,x_3) \\ &= 32.247987 + 0.016811x_1^2 + 0.000331x_2^2 + 0.03225x_3^2 \\ &\quad -0.315994x_1 + 0.062161x_2 - 0.104718x_3 \\ &\quad -0.007409x_1x_2 - 0.001306x_1x_3 + 0.01523x_2x_3 \end{aligned} \tag{18}$$

$$\begin{aligned} &T_{avg}(n,d,h) = F_2(x_1,x_2,x_3) \\ &= 30.975572 + 0.013209x_1^2 + 0.0036x_2^2 - 0.022x_3^2 \\ &\quad -0.331968x_1 - 0.079503x_2 + 0.053948x_3 \\ &\quad -0.00136x_1x_2 - 0.001923x_1x_3 + 0.0247x_2x_3 \end{aligned} \tag{19}$$

$$\begin{aligned} &\Delta P(n,d,h) = F_3(x_1,x_2,x_3) \\ &= 1466.492828 - 0.357566x_1^2 + 3.26915x_2^2 + 128.1997x_3^2 \\ &\quad +52.214524x_1 - 90.969828x_2 - 836.628689x_3 \\ &\quad -2.92262x_1x_2 - 5.549175x_1x_3 + 16.2774x_2x_3 \end{aligned} \tag{20}$$

R^2 represents the model's goodness of fit. The fitting accuracy for T_{max}, T_{avg}, and ΔP are 0.994, 0.998, and 0.993, respectively, indicating that the surrogate models for the objective functions have a high degree of accuracy and can effectively replace numerical simulations.

Based on the fitted surrogate models and the NSGA-II algorithm, the multi-objective optimization design mathematical model for the arch-shaped channel structure parameters is formulated as follows:

$$\min F(x_1,x_2,x_3) = \begin{cases} \min F_1(x_1,x_2,x_3) \\ \min F_2(x_1,x_2,x_3) \\ \min F_3(x_1,x_2,x_3) \end{cases} Subject to \begin{cases} 6 \le x_1 \le 12 \\ 7 \le x_2 \le 10 \\ 1.5 \le x_3 \le 3 \end{cases} \tag{21}$$

The NSGA-II is implemented by programming, considering computational resources and time. The initial population size is set to 100 individuals, and the maximum number of generations is set to 100 steps within a reasonable range. Based on experience, a mutation probability of 0.02 is chosen. Fig. 9 shows the Pareto optimal set of objective functions obtained using the NSGA-II. From the optimal solution set, it can be seen that the performance indicators of each objective function are mutually constrained. Improving one indicator always comes at the cost of sacrificing others, so temperature and ΔP are mutually constrained. In the Pareto optimal solution set, each solution is a global

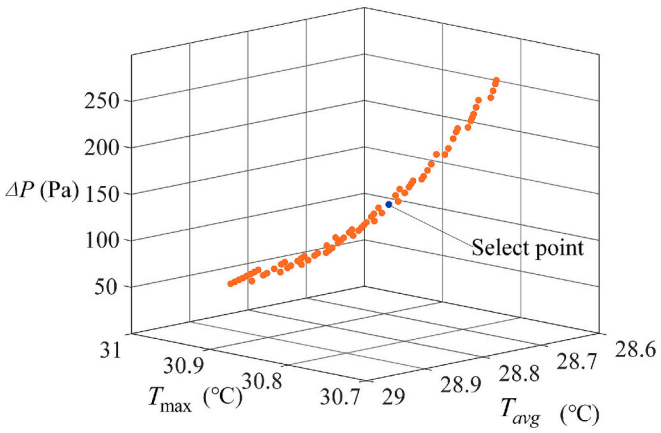

Fig. 9. Pareto optimal solution sets.

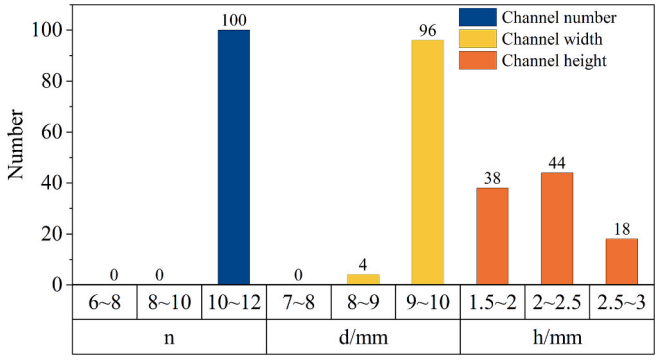

Fig. 10. Proportion of intervals for each variable.

Pareto optimal solution. The solution set is then statistically organized according to the range of each design variable, as shown in Fig. 10. Based on the proportions of solutions in each interval, the final optimized design result is selected: $n = 12$ mm, $d = 9.4$ mm, and $h = 2.1$ mm.

3.8. Comparison of results

Based on the results obtained from the orthogonal experiment and NSGA-II optimization, a 3D model is constructed and subjected to numerical analysis. A comparative analysis of the temperature and velocity contour maps of the cold plate before and after optimization in Fig. 11, as well as the data graphs in Fig. 12, reveals that the cold plate optimized using the genetic algorithm exhibits fewer high-temperature accumulation zones and a lower fluid velocity, resulting in a reduction in ΔP. Consequently, the OSCP demonstrates enhanced heat dissipation performance and reduced pump power consumption. As shown in Fig. 12, the optimized cold plate experiences a 0.14 °C decrease in T_{max}, a 0.29 °C reduction in T_{avg}, and a 17.66 Pa reduction in ΔP compared to the initial configuration.

4. Topology optimization

4.1. Topology model design and boundary conditions

In typical cold plate topology optimization, the design variables are typically calculated and solved using a uniform density field with a design variable value of 0.5. In this study, the geometric parameters of OSCP are used as the initial solution for the topology optimization design, resulting in the TSCP. As shown in Fig. 13, the dimensions of the topology optimization design domain are 2.2 L in length and 1.36 L in width. The dimensions of both the fluid inlet and outlet are 0.15 L ×

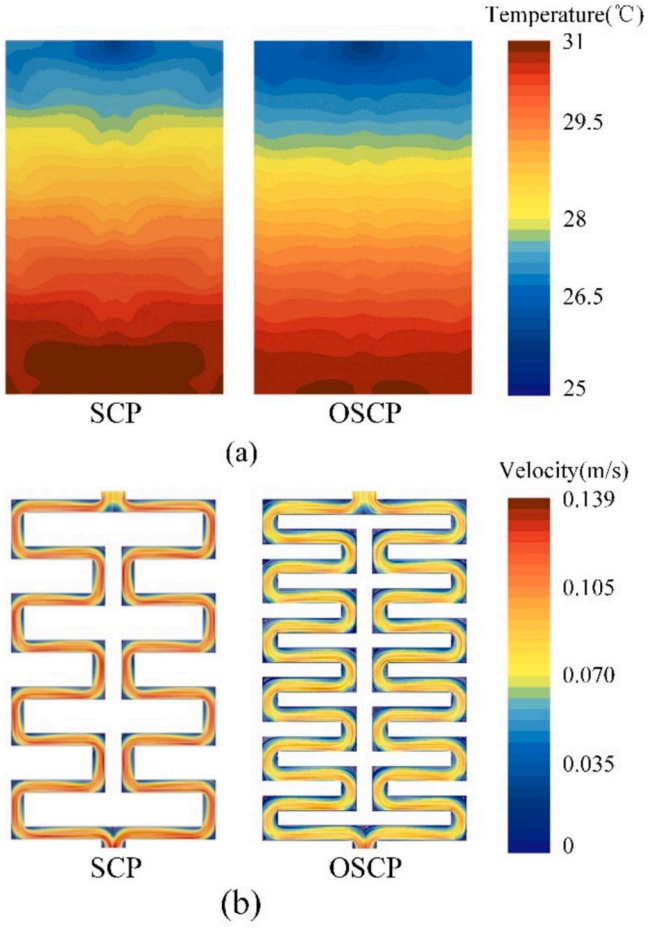

Fig. 11. Comparison analysis of SCP and OSCP: (a) Temperature cloud map; (b) velocity cloud map.

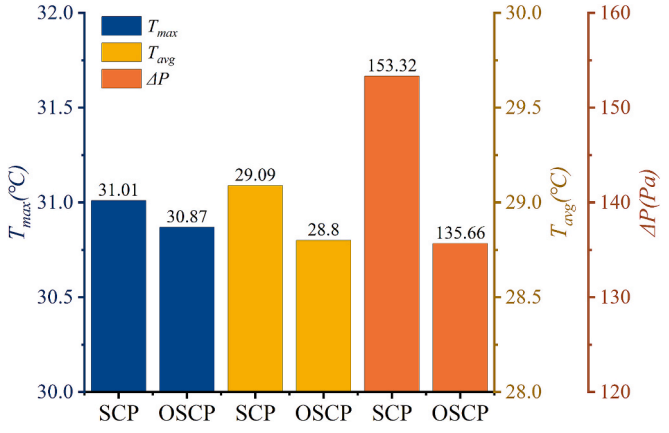

Fig. 12. Data comparison of SCP and OSCP.

0.15 L, where L is the dimensionless unit length. The initial solution design is carried out based on the geometric parameters of the TSCP as shown in Fig. 12a, such that the element density γ of the channels in the OSCP is 1, representing the fluid domain, while for the remaining parts, γ = 0, representing the solid domain. In Fig. 12b, the entire design domain is a uniform density field with an element density γ = 0.5. To ensure fairness in the design, the volume fraction of the fluid domain in the OSCP is used to constrain the volume fraction of the volume domain for the initialized topology optimization and direct topology optimization. The remaining boundary conditions are consistent with those described earlier.

4.2. Governing equations

4.2.1. Flow equation

Assuming incompressible, steady-state, laminar fluid flow, the governing equations are represented by the dimensionless continuity equation and the Navier-Stokes (N-S) equations [46]:

$$\nabla^{*}\cdot u^{*}=0 \tag{22}$$

$$\rho(u^{*}\cdot\nabla^{*})u^{*}=-\nabla P+\mu\nabla^{2}u^{*}+F \tag{23}$$

where u is the velocity vector, P is the pressure, and μ is the dynamic viscosity. The dimensionless transformation equations are as follows:

$$\nabla^{*}=L\nabla,\boldsymbol{u}^{*}=\frac{u}{U},p^{*}=\frac{p-p_{0}}{\rho U^{2}},Re=\frac{\rho UL}{\mu} \tag{24}$$

where ∇ is the dimensionless gradient operator, L is the characteristic length, u^{*} is the dimensionless velocity, and u^{*} is the dimensionless pressure.

F is the body force during the flow process, and the equation (25) is derived from the Brinkman penalty model. α is the dimensional permeability, which is associated with the design variable γ and can be expressed using an interpolation function as [47]:

$$F=-\alpha u^{*} \tag{25}$$

$$\alpha(x)=\alpha_{\max}\frac{q(1-\gamma)}{q+\gamma} \tag{26}$$

$$\alpha_{\max}=(1+\frac{1}{\mathrm{Re}})Da \tag{27}$$

where q is the penalty factor, which is set to 10^{-2} in this study, and Da is the Darcy number, set to 10^{-4} in this study.

The dimensionless continuity equation and energy equation are thus obtained as follows:

$$\nabla^{*}\cdot u^{*}=0 \tag{28}$$

$$\rho(u^{*}\cdot\nabla^{*})u^{*}=-\nabla^{*}P^{*}+\frac{1}{\mathrm{Re}}\nabla^{*2}u^{*}-\frac{1}{Da}(1+\frac{1}{\mathrm{Re}})\frac{q(1-\gamma)}{q+\gamma}u^{*} \tag{29}$$

4.2.2. Heat transfer model

Considering the heat transfer characteristics of both solid and liquid phases, the heat transfer equation is expressed as [48]:

$$\mathrm{Re}Pr(u^{*}\cdot\nabla^{*})T^{*}=\nabla^{*2}T^{*}\ \text{Fluid domains} \tag{30}$$

$$0=\nabla^{*2}T^{*}+Q^{*}\text{Solid domains} \tag{31}$$

where Pr is the Prandtl number, which is set to 6.78 (at standard temperature and pressure) in this study, Q^{*} is the dimensionless heat generation rate, and T^{*} is the dimensionless temperature. According to Newton's law of cooling, the following equation is obtained:

$$Q^{*}=\mathrm{h}^{*}(1-T^{*}) \tag{32}$$

The integrated equation, which is applicable to both the fluid domain and the solid domain, is obtained as follows:

$$\gamma\mathrm{Re}Pr(u^{*}\cdot\nabla^{*})T^{*}=\nabla^{*2}T^{*}+(1-\gamma)h^{*}(1-T^{*}) \tag{33}$$

The dimensionless transformation equation is as follows:

$$T^{*}=\frac{T-T_{e}}{T_{a}-T_{e}},\ Pr=\frac{\mu C_{p}}{k_{f}},\ h^{*}=\frac{hL^{2}}{k_{f}} \tag{34}$$

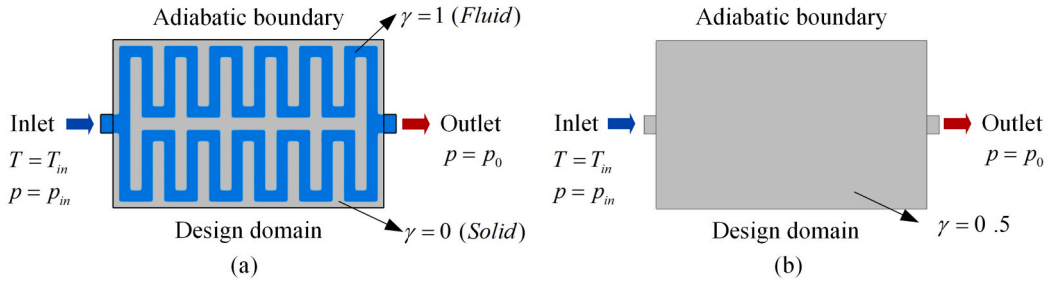

Fig. 13. Initial geometric model and boundary conditions: (a) TSCP; (b) TCP.

where T_a is the average temperature, T_e is the reference temperature, C_p is the specific heat capacity, h is the heat generation coefficient, and k_f is the thermal conductivity of the fluid.

4.2.3. Filtering and projection

The density filtering in the form of the Helmholtz partial differential equation can improve the numerical stability of the solution and avoid dependence on the mesh that may affect the topology [30]:

$$-R^2\nabla^2\widetilde{\gamma}+\widetilde{\gamma}=\gamma \tag{35}$$

where γ is the design variable before filtering, $\widetilde{\gamma}$ is the design variable after filtering, and R is the filtering radius.

The use of hyperbolic tangent projection can address the issue of gray cells resulting from density filtering, thereby enhancing the clarity of the flow channels generated by the topology [31]:

$$\gamma_0=\frac{(\tanh(\beta(\widetilde{\gamma}-\gamma_\beta))+\tanh(\beta\gamma_\beta))}{(\tanh(\beta(1-\gamma_\beta))+\tanh(\beta\gamma_\beta))} \tag{36}$$

where γ_0 is the design variable after projection, γ_β is the projection point, and β is the slope. In this study, γ_β is set to 0.5, and β is set to 8.

4.2.4. Objective function

This study defines a bi-objective function with the goals of maximizing heat transfer and minimizing dissipation power. Under steady-state conditions, heat generation equals heat transfer. The objective function for maximizing heat transfer can be expressed as:

$$J_1=\int_\Omega(1-\gamma)h^*(1-T^*)d\Omega \tag{37}$$

The minimization of dissipation power can be expressed by the following equation:

$$J_2=\int_\Omega\left[\nabla^*u^*\cdot\left(\nabla^*u^*+\nabla^*u^{*T}\right)+\alpha^*u^*\cdot u^*\right]d\Omega \tag{38}$$

To represent the multi-objective function, it can be expressed using a weighted sum method through linear combination, satisfying $\omega_1+\omega_2=1$. The minimum value of the optimization objective can be represented as Φ:

$$\Phi=-w_1J_1+w_2J_2 \tag{39}$$

Considering the boundary condition issues, the multi-objective problem can ultimately be expressed as:

$$\begin{aligned}&Find\gamma_i(i=1,2,\ldots,N)\\&Minmize\Phi=-w_1J_1+w_2J_2\\&Subjectto\begin{cases}\int_{\Gamma_n}p_{in}^*\boldsymbol{u}^*d\Gamma=1\\\dfrac{\int_\Omega\gamma d\Omega}{\int_\Omega 1d\Omega}=V_f\\0\le\gamma_i\le1(i=1,2,\cdots,N)\end{cases}\end{aligned} \tag{40}$$

4.3. Parameter definition

The pump power is used to evaluate the power required to drive the coolant by the P_{pump} [30]:

$$P_{pump}=\Delta PQ_m/\rho_f \tag{41}$$

where Q_m refers to the mass flow rate.

The commonly used dimensionless performance evaluation factor j/f is used to assess the heat dissipation and hydraulic performance of the cold plate [49]. The Colburn factor j represents the dimensionless heat transfer capacity of the cooling plate surface, and it is expressed as:

$$j=\frac{Nu}{\boldsymbol{RePr}^{1/3}} \tag{42}$$

The Nusselt number is typically expressed as:

$$Nu=\frac{h_cD_h}{\lambda_f} \tag{43}$$

The fluid convective heat transfer coefficient is defined as follows:

$$h_c=\frac{C_{\rho,f}Q_m(T_{out}-T_{in})}{A_{f,w}(T_{f,w}-\frac{T_{in}+T_{out}}{2})} \tag{44}$$

where T_{in} is the inlet temperature, T_{out} is the outlet temperature, and $T_{f,w}$ is the average wetted surface temperature.

The flow resistance coefficient f is used to characterize the fluid flow resistance and can be expressed as:

$$f=\frac{1}{2}\frac{D_h}{L_1}\frac{\Delta P}{\rho_fu_{in}^2} \tag{45}$$

where L_1 is the equivalent length of the channel.

4.4. Topology optimization process

To perform the topology optimization design, a 2D cold plate model is first established. Computational fluid dynamics (CFD) is then applied to solve the laminar flow model, while Conjugate Heat Transfer is utilized to address the heat transfer problem. After defining the appropriate boundary conditions and parameters, the next step is to formulate the optimization objective function. SNOPT with the advantages of high efficiency and accuracy is selected as the solver for solving. The iteration termination criterion is set as $\Phi_k+\Phi_{k+1}\le10^{-6}$ (k is the number of iterations). The iteration process is shown in Fig. 14. It can be observed that the initialized topology optimization converges faster compared to the direct topology optimization.

4.5. Topology optimization results selection

As the Reynolds number changes, the topology results also vary. Fig. 15 shows the topology results for Reynolds numbers ranging from 150 to 300. For TSCP, as the Reynolds number increases, the width of

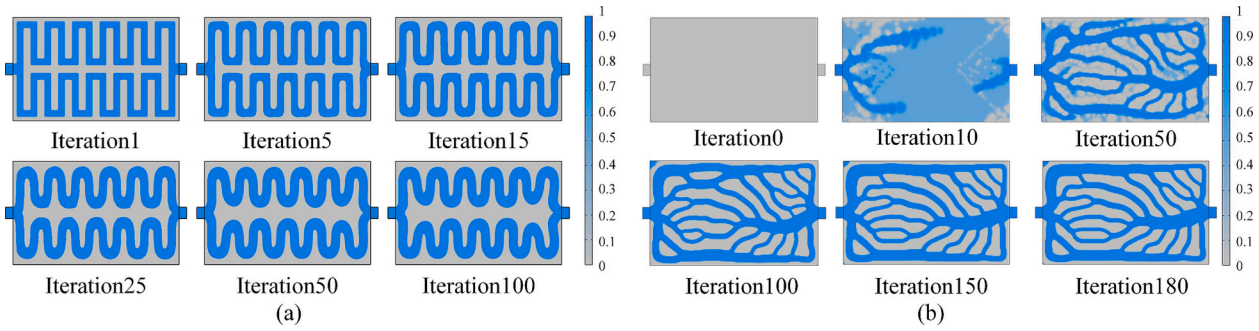

Fig. 14. Topology iteration process: (a) TSCP; (b) TCP.

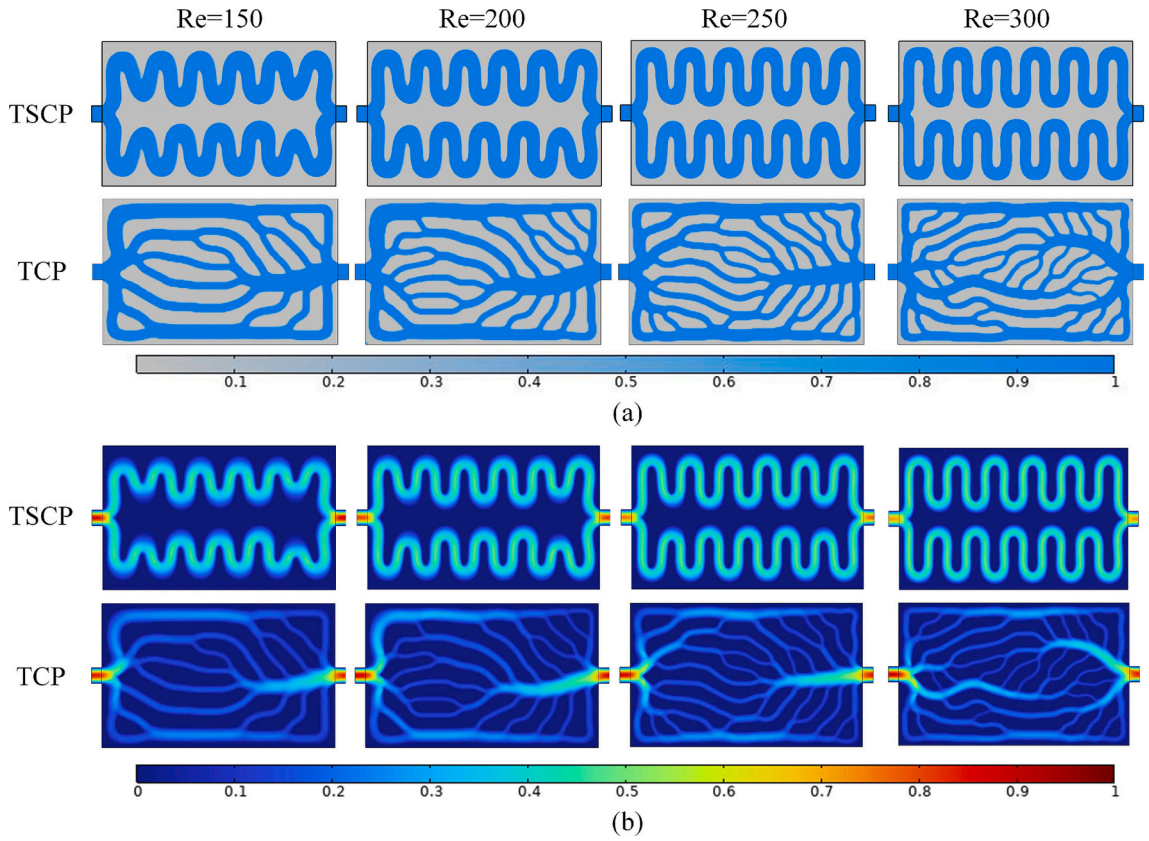

Fig. 15. Topology results at different reynolds numbers: (a) Topology structures; (b) velocity cloud map.

the flow channels decreases, the amplitude of the turns increases, and the angle between the two channels becomes smaller, tending toward parallelism. For TCP, as the Reynolds number increases, the flow channel width gradually narrows, and smaller channels appear. When the Reynolds number reaches 300, the complexity of the flow channels significantly increases. However, when the Reynolds number increases from 250 to 300, the changes in the flow channels become minimal. In the velocity cloud map shown in Fig. 15(b), For TSCP, as the Reynolds number increases, the channel structure becomes steeper, the fluid velocity within the channels increases, and the high-speed region at the turns expands. For TCP, the high-speed region is mainly concentrated in the middle of the main channel and at the entrances of some branch channels. As the Reynolds number increases, the flow velocity further increases, but the distribution becomes more uniform, and the network becomes more intricate. However, the complexity of the flow channel structure leads to a significant increase in manufacturing costs. Considering all factors, the topology structure at a Reynolds number of 250 is selected for further discussion.

4.6. Analysis of TSCP topology results

Topology optimization was performed on all the structures in the orthogonal experimental group, and the results are shown in Fig. 16. It was found that under different channel numbers and parameter combinations, the design results from the topology optimization method all exhibited streamlined structures. From the topology optimization results, it can be observed that, driven by the objective function, the rectangular channels tend to transform into a streamlined shape, resembling the commonly used traditional serpentine structure, but with some differences. In traditional serpentine structures, the parameters are subject to predefined constraints, such as the length, width, and turning radius at the corners, which need to be specified in the early stages of the design. Although these parameterized constraints simplify the design process, they also limit the exploration of the design space, potentially confining the optimization results to pre-set geometric forms, thus failing to fully tap into the potential performance enhancement of the liquid cooling system. By redesigning under the objective function, the

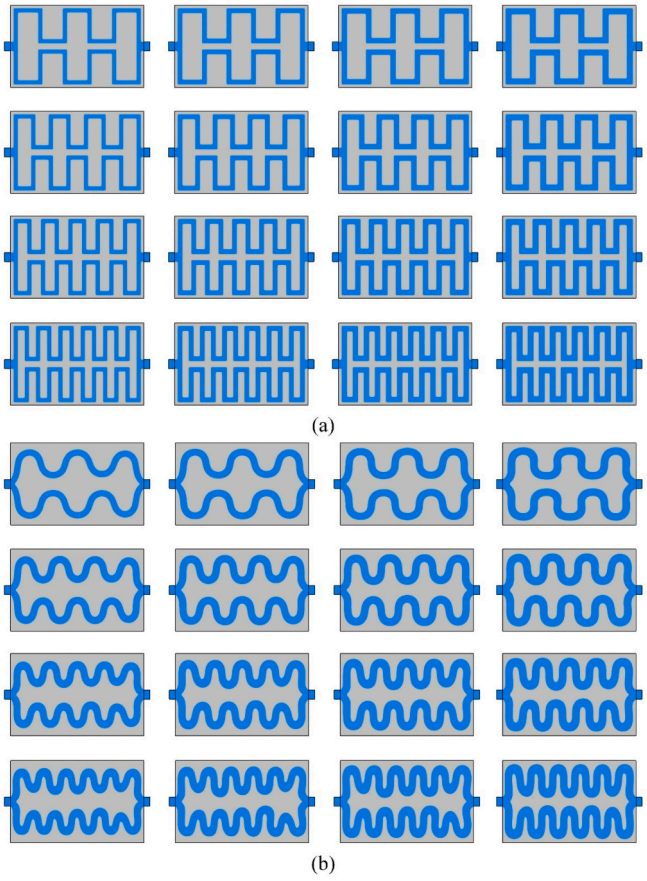

Fig. 16. Comparison before and after topology optimization: (a) Initial structures; (b) topology structures.

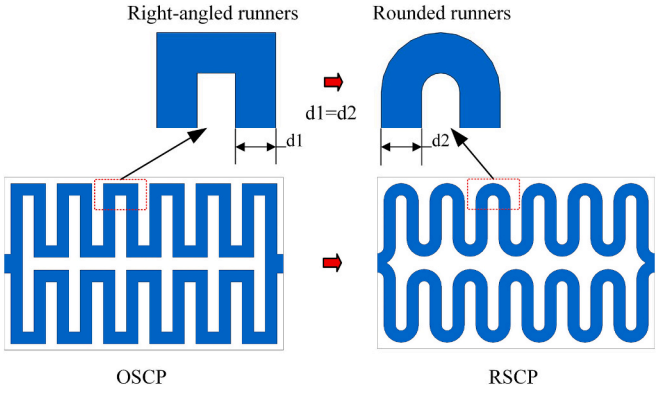

Fig. 17. Transition from OSCP to RSCP.

channel distribution found within the design domain ultimately forms this streamlined channel shape, similar to the traditional serpentine structure. To better verify the effectiveness of the topology optimization method, a traditional rounded-corner serpentine structure (RSCP), as shown in Fig. 17, is introduced. The channel width and height of the RSCP are kept consistent with those of the OSCP for a fair comparison and evaluation.

4.7. Results and discussion

The initialization topology optimization results for RSCP are similar to those based on OSCP, and thus will not be discussed here. Therefore, the flow characteristics and thermal properties will be analyzed only for the four structures: TSCP, OSCP, RSCP and TCP, as shown in Fig. 18.

4.7.1. Flow characteristics analysis

Fig. 19(a) shows the variation of the flow resistance coefficient with increasing mass flow rate. As the mass flow rate increases, the flow resistance coefficient for all four cold plate structures decreases nonlinearly, with the rate of decrease gradually slowing after 3 g/s. TCP exhibits the lowest flow resistance, benefiting from its branched structure that distributes the fluid evenly across multiple channels. Among the serpentine channels, TSCP shows a significant reduction in flow resistance compared to OSCP and RSCP, demonstrating the effectiveness of the initialization-based topology optimization in enhancing serpentine channel performance. Fig. 19(b) presents the change in pump power consumption with increasing mass flow rate. The pump power consumption rises approximately exponentially as the mass flow rate increases. TCP consumes the least pump power, where the reduction in flow resistance directly translates into lower energy demands. However, the high geometric complexity of TCP's channel network increases manufacturing challenges, which must be considered in practical applications. Among the serpentine channels, With varying mass flow rates, TSCP reduces P_{pump} by 38.82 % to 52.47 % compared to OSCP, while RSCP reduces P_{pump} by 3.44 % to 21.26 % compared to OSCP, depending on the mass flow rate. Although RSCP also shows improvements over OSCP, the optimization effect is less significant than that of TSCP, highlighting the advantage of the initialization-based topology optimization method in reducing energy consumption.

4.7.2. Thermal characteristics analysis

As observed in Fig. 20, both T_{max} and T_{avg} of the battery exhibit a decreasing trend with the increase in mass flow rate or pump power. Within a certain range, the decrease in T_{max} and T_{avg} is pronounced; however, as these variables continue to increase, the rate of decrease in T_{max} and T_{avg} slows down. This suggests that while increasing the mass flow rate or pump power can improve the thermal performance of the cold plate, the enhancement in heat dissipation capacity is limited and cannot continue to increase indefinitely.

Fig. 20(a) illustrates the variation of T_{max} with increasing mass flow rate for TSCP, OSCP, RSCP, and TCP. At lower mass flow rates, the maximum temperatures of TSCP, OSCP, and RSCP show little difference. As the mass flow rate continues to increase, noticeable differences begin to appear after 3 g/s, although the overall variation remains small. TCP

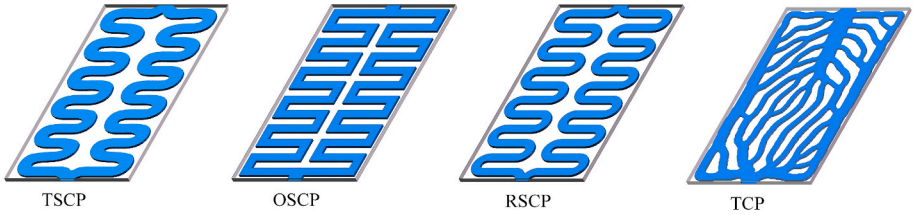

Fig. 18. Four structures: TSCP, OSCP, RSCP and TCP.

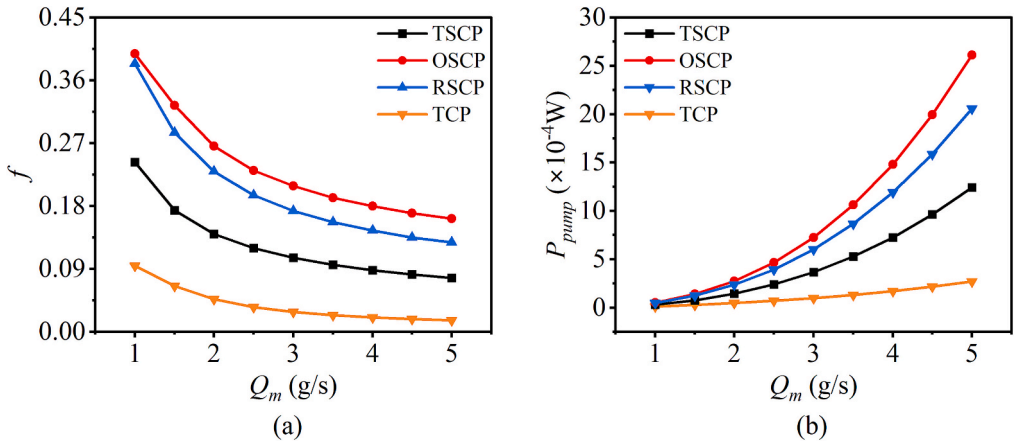

Fig. 19. Flow performance comparison of TSCP, OSCP, RSCP and TCP: (a) f; (b) P_{pump}.

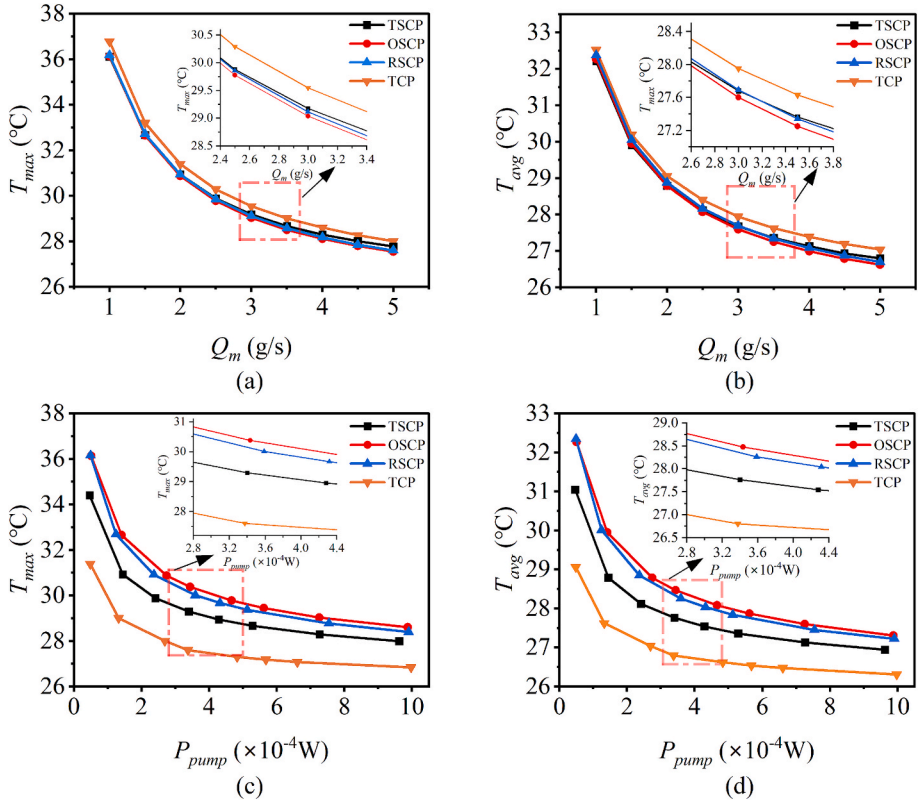

Fig. 20. Thermal characteristics comparison of TSCP, OSCP, RSCP and TCP: (a) T_{max} variation with Q_m. (b) T_{avg} variation with Q_m; (c) T_{max} variation with P_{pump}; (d) T_{avg} variation with P_{pump}.

exhibits a generally higher T_{max} compared to TSCP, OSCP, and RSCP, while OSCP maintains the lowest T_{max}. At a mass flow rate of 5 g/s, OSCP's T_{max} is 0.22 °C lower than that of TSCP, 0.05 °C lower than RSCP, and 0.46 °C lower than TCP. Fig. 20(b) presents the variation of T_{avg} with increasing mass flow rate. At lower mass flow rates, there is no significant difference in T_{avg} among TSCP, OSCP, and RSCP. A turning point appears at 3 g/s, after which more noticeable differences emerge as the mass flow rate exceeds 3 g/s; however, the overall variation among TSCP, OSCP, and RSCP remains relatively small. In contrast, the difference between TCP and the other three structures gradually increases, with TCP showing a higher T_{avg}. At a mass flow rate of 5 g/s, OSCP's T_{avg} is 0.17 °C lower than that of TSCP, 0.07 °C lower than RSCP, and 0.41 °C lower than TCP.

In the flow analysis, it was found that TCP exhibits a significant advantage in reducing energy consumption, while TSCP also shows lower energy consumption compared to OSCP and RSCP at the same mass flow rate. Moreover, in practical engineering applications, more attention is paid to achieving lower temperatures under a given pump power. Fig. 20(c) and (d) present the variations of T_{max} and T_{avg} for TSCP, OSCP, RSCP, and TCP at the same pump power. From the trends, it can be observed that with the increase of pump power, the thermal performance of the cold plates improves, as evidenced by the decrease in both T_{max} and T_{avg}. TCP shows a significant advantage in terms of both T_{max} and T_{avg}, while TSCP also exhibits clear differences compared to OSCP and RSCP. When the pump power is 3.4×10^{-4} W, the T_{max} of TCP is 2.78 °C lower than that of OSCP, and the T_{avg} of TCP is 1.67 °C lower than that of OSCP; the T_{max} of TSCP is 1.08 °C lower than OSCP and 0.84 °C lower than RSCP, while the T_{avg} of TSCP is 0.71 °C lower than

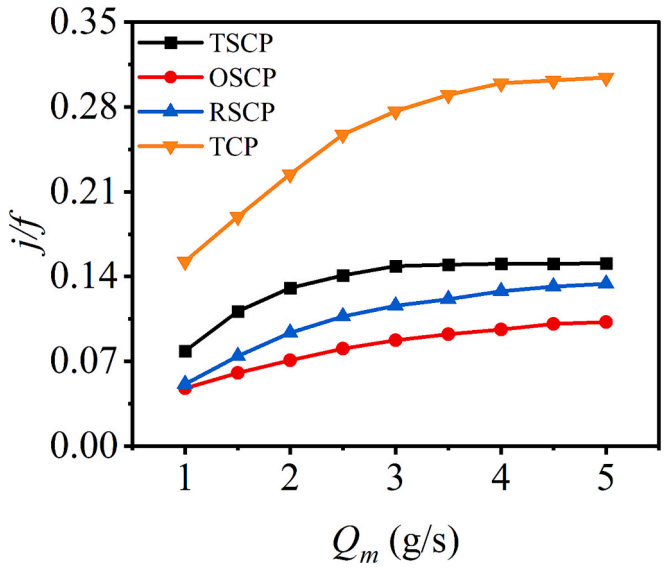

Fig. 21. Comprehensive evaluation comparison of TSCP, OSCP, RSCP and TCP.

Table 8
Data Comparison of TSCP, OSCP, RSCP and TCP.

	TSCP	OSCP	RSCP	TCP
T_{max}	29.17	29.04	29.11	29.55
T_{avg}	27.68	27.60	27.67	27.95
ΔP	122.39	241.38	200.41	32.97
j/f	0.1486	0.0875	0.116	0.276

OSCP and 0.58 °C lower than RSCP. However, the cooling performance does not improve indefinitely with increasing pump power. When the pump power is below 4×10^{-4} W, the improvement trend is evident, whereas beyond this point, the performance enhancement diminishes as the pump power continues to increase.

4.7.3. Comprehensive evaluation analysis

To strike a balance between cooling performance and pump power consumption, the j/f comprehensive evaluation factor is employed to assess the overall performance of the three cold plate structures, where a higher j/f value indicates better overall performance. The variation of j/f with mass flow rate is shown in Fig. 21. The j/f value increases nonlinearly with the increase in mass flow rate, with a more significant growth trend observed when the mass flow rate is below 3 g/s, and a slower growth trend beyond this point. TCP consistently maintains the highest j/f value, demonstrating the overall advantage of the topology optimization method in balancing heat transfer and energy consumption, primarily reflected in its low energy consumption. TSCP also exhibits outstanding performance within the serpentine structure, with its j/f value showing significant improvement compared to OSCP and RSCP, indicating that the initialization-based topology optimization effectively enhances the comprehensive performance of the traditional serpentine cold plate.

Based on the trend shown in Fig. 21, this study selects the results at a mass flow rate of 3 g/s for comparison. The numerical results are shown in Table 8. Fig. 22(a) presents the temperature cloud maps of the cross-sections of the cold plates for the TSCP, OSCP, RSCP, and TCP. The four structures exhibit similar temperature distribution trends, with temperature gradually increasing from the inlet to the outlet, and heat accumulation mainly occurring near the outlet. TCP shows a relatively higher temperature. Fig. 22(b) illustrates the ΔP distributions for the four structures. The results indicate that TCP exhibits the lowest pressure drop, suggesting that the complex branched structure formed through free topology optimization effectively achieves uniform fluid distribution and significantly reduces overall flow resistance. TSCP also shows a significantly lower ΔP compared to RSCP and OSCP, indicating that initialization-based topology optimization effectively reduces pressure drop while maintaining the serpentine structure. RSCP exhibits a slightly lower ΔP than OSCP, though the improvement is less pronounced than that of TSCP. Fig. 22(c) displays the velocity cloud maps, where it can be observed that the TCP structure features multiple branches at the inlet and outlet, leading to a uniform velocity distribution. The transitions between the main channel and branches are smooth, with minimal impact or backflow phenomena, effectively reducing flow dead zones and local high-velocity scouring, and significantly lowering pumping power. In TSCP, the structural design around the inlet and outlet mitigates flow impacts, optimizes the ΔP at these points, and the corner transitions within the flow paths are more gradual, reducing flow resistance and effectively decreasing pumping power. From a structural perspective, compared to TSCP and RSCP, OSCP generates vortices during fluid flow through the channels, increasing fluid disturbances, disrupting the boundary layer, and enhancing heat transfer between the fluid and the wall. However, this also results in a higher ΔP within the channel, increasing energy losses. In contrast, TSCP's channels do not generate vortices, leading to relatively poorer heat transfer, but providing more stable flow characteristics and significantly lower ΔP. In terms of the j/f comprehensive evaluation index, TCP exhibits the highest j/f value among all structures, demonstrating the best overall performance in balancing heat transfer and low pressure drop. Within the serpentine cold plates, the j/f value of TSCP is 69.76 % higher than that of OSCP and 28.45 % higher than that of RSCP. In summary, TCP, relying on a branched network formed through free topology optimization, significantly reduces flow resistance, resulting in a very low friction factor (f) and achieving a substantial advantage in the comprehensive performance index. However, due to its high geometric complexity, TCP entails greater manufacturing and maintenance costs, posing challenges for practical engineering applications. In contrast, TSCP, developed by applying topology optimization based on the OSCP as the initial structure, features a simpler geometry and lower manufacturing costs. It effectively improves flow resistance and reduces pressure drop, thereby decreasing pumping power consumption. These results demonstrate the feasibility of this new serpentine cold plate design method in enhancing the overall performance of SCPs.

5. Conclusion

This paper proposes a novel design method for serpentine cold plates, leading to the development of a new serpentine cold plate structure, TSCP. The method initially employs orthogonal experimental design and the NSGA-II multi-objective optimization algorithm to derive the traditionally optimized structure, OSCP. Subsequently, OSCP is used as the initial design for topology optimization, aiming to maximize heat transfer and minimize dissipation power, resulting in the superior new serpentine cold plate, TSCP. To comprehensively assess the overall performance of TSCP, numerical simulation analyses are conducted, comparing TSCP with the traditionally optimized OSCP, the conventional rounded serpentine cold plate (RSCP), and the freely structured cold plate derived from direct topology optimization (TCP). The key conclusions are as follows:

(1) The proposed design method for serpentine cold plates combines traditional parameter optimization with topology optimization, fully leveraging the heat dissipation advantages of the serpentine structure, particularly effectively alleviating the high pressure drop and excessive pump power consumption issues typically associated with traditional serpentine cold plates.
(2) At a mass flow rate of 3 g/s, the pump power of TSCP is reduced by 49.3 % compared to OSCP, while RSCP shows a reduction of

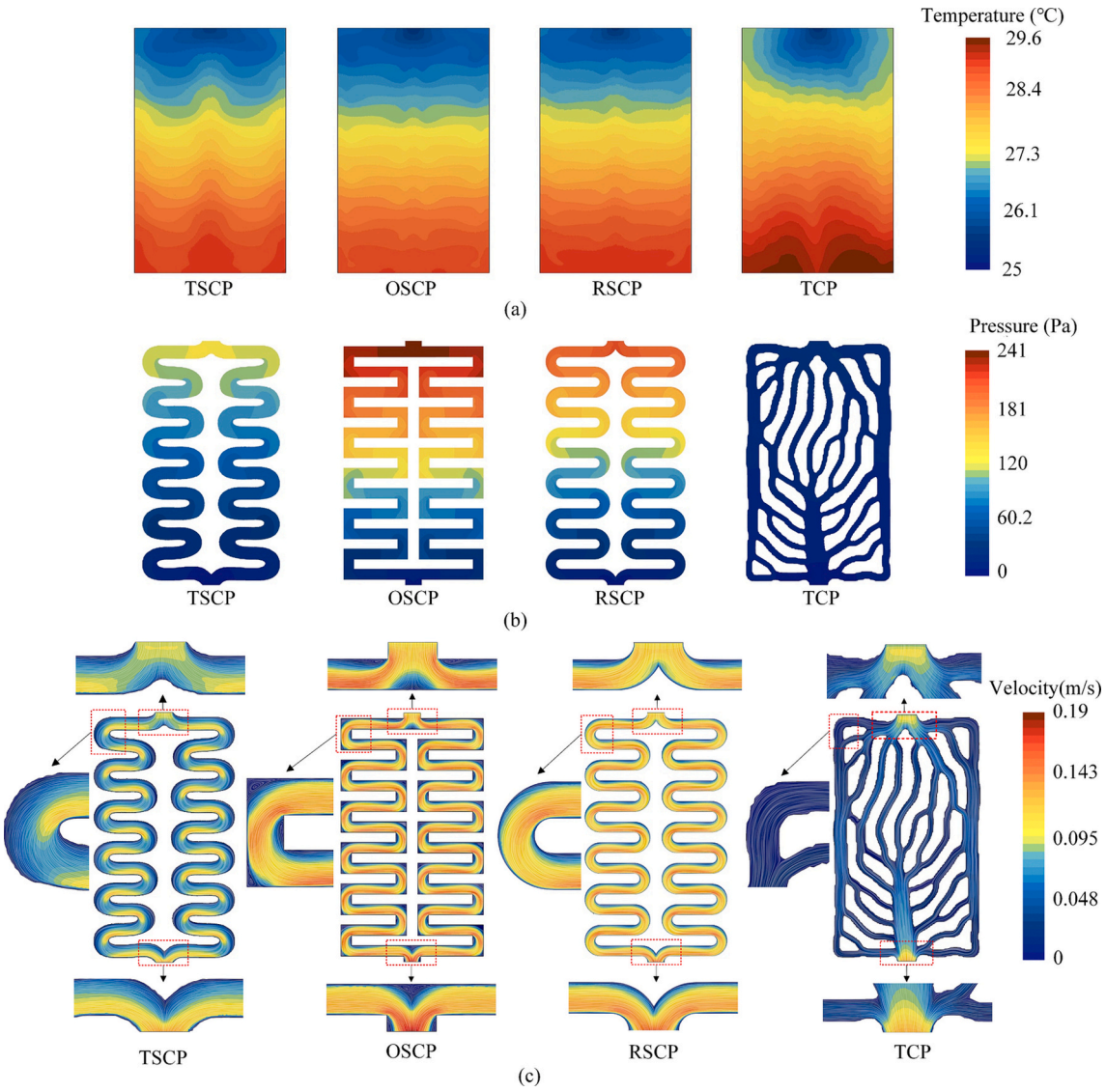

Fig. 22. Results analysis of TSCP, OSCP, RSCP and TCP: (a) Temperature cloud map; (b) pressure cloud map; (c) velocity cloud map.

15.34 % compared to OSCP. TSCP significantly reduces pump power consumption while ensuring effective heat dissipation.

(3) At a mass flow rate of 3 g/s, TSCP shows a notable improvement in overall performance, with its *j/f* value increasing by 69.76 % compared to OSCP and by 28.45 % compared to RSCP. This indicates that the proposed design method significantly enhances the overall performance of the serpentine cold plate.

(4) The TCP exhibits the best overall performance metrics due to its lower flow resistance. However, its complex multi-branch structure significantly increases manufacturing difficulty and cost. In contrast, the TSCP maintains excellent thermal performance while effectively avoiding the overly complex structures often generated by direct topology optimization, and also improves the convergence efficiency of the optimization process.

CRediT authorship contribution statement

Sen Zhan: Conceptualization, Methodology, Investigation, Writing – original draft, Project administration. **Xingyu Zhao:** Methodology, Data curation, Visualization, Writing – review & editing. **Shuen Zhao:** Formal analysis, Writing – review & editing. **Shaojiang Dong:** Investigation, Supervision. **Yanli Yin:** Resources, Funding acquisition.

Declaration of competing interest

The authors declare that they have no known competing financial interests or personal relationships that could have appeared to influence the work reported in this paper.

Acknowledgements

This work was supported by the Technological Innovation and Application Development Research Program of the Chongqing Municipal Science and Technology Commission (Grant number: cstc2020jscx-dxwtBX0025), Open Foundation of State Key Laboratory of Mechanical Transmission (Grant number: SKLMT-MSKFKT-202112), Chongqing Key Laboratory of Urban Rail Transit System Integration and Control Open Fund (Grant number: CKLURTSIC-KFKT-212001), Chongqing Natural Science Foundation Innovation and Development Joint Fund (Grant number: CSTB2024NSCQ-LZX0105), and Chongqing Jiaotong University Natural Science Category Unveiling and Commanding Project: Theoretical Research on Vehicle-Road-Cloud Integrated Perception and Collaborative Control for Intelligent Connected Driving (XJ2023).

Data availability

No data was used for the research described in the article.

References

[1] H. Li, L. Chen, H. Zuo, B. Zhang, G. Jia, Performance enhancement of a battery thermal management system using novel liquid cold plates with micro-channel featuring pin fins, Energy 301 (2024) 131731, https://doi.org/10.1016/j.energy.2024.131731.

[2] H. Ji, T. Luo, L. Dai, Z. He, Q. Wang, Topology design of cold plates for pouch battery thermal management considering heat distribution characteristics, Appl. Therm. Eng. 224 (2023) 119940, https://doi.org/10.1016/j.applthermaleng.2022.119940.

[3] Y. Yang, R. Wang, Z. Shen, Q. Yu, R. Xiong, W. Shen, Towards a safer lithium-ion batteries: a critical review on cause, characteristics, warning and disposal strategy for thermal runaway, Adv. Appl. Energy 11 (2023) 100146, https://doi.org/10.1016/j.adapen.2023.100146.

[4] X. Zhu, X. Liao, S. Kang, L. Sun, Y. Zhao, Optimization design of lithium battery management system based on Z-F composite air cooling structure, J. Storage Mater. 102 (2024) 114068, https://doi.org/10.1016/j.est.2024.114068.

[5] A.B. Padalkar, M.B. Chaudhari, K.B. Kore, S.R. Newaskar, D.S. Nilegave, A. M. Funde, Effects of circumferential fin on cooling performance improvement of forced air-cooled battery pack, Appl. Therm. Eng. 238 (2024) 122013, https://doi.org/10.1016/j.applthermaleng.2023.122013.

[6] S. Zhan, Z. Cheng, Y. Yin, C. Yu, C. Zhao, Effect of inlet and outlet positions on heat dissipation performance of lithium-ion battery cold plates: an analysis based on topology optimization, Int. J. Heat Mass Transf. 215 (2023) 124436, https://doi.org/10.1016/j.ijheatmasstransfer. 2023.124436.

[7] C. Chen, Y. Qian, G. Xu, Q. Zhang, P. Lu, Numerical investigation on thermal management performance of soft packing Li-ion batteries with oblique multi-channel cold plates, Renew. Energy 234 (2024) 121250, https://doi.org/10.1016/j.renene.2024.121250.

[8] H. Yang, M. Li, Z. Wang, B. Ma, A compact and lightweight hybrid liquid cooling system coupling with Z-type cold plates and PCM composite for battery thermal management, Energy 263 (2023) 126026, https://doi.org/10.1016/j.energy.2022.126026.

[9] A. Moaveni, M. Siavashi, S. Mousavi, Passive and hybrid battery thermal management system by cooling flow control, employing nano-PCM, fins, and metal foam, Energy 288 (2024) 129809, https://doi.org/10.1016/j.energy.2023.129809.

[10] J. Kleiner, F. Lambauer, R. Singh, L. Komsiyska, M. Hinterberger, C. Endisch, Experimental study of cell integrated heat pipe cooling with a lithium-ion cell emulator, J. Storage Mater. 56 (2022) 105808, https://doi.org/10.1016/j.est.2022.105808.

[11] W. Zhang, Q. Sun, X. Zhou, L. Wu, Y. Hu, Investigation on the thermal behavior of thermal management system for battery pack with heat pipe based on multiphysics coupling model, Energy 308 (2024) 133053, https://doi.org/10.1016/j.energy.2024.133053.

[12] G. Zhao, X. Wang, M. Negnevitsky, C. Li, An up-to-date review on the design improvement and optimization of the liquid-cooling battery thermal management system for electric vehicles, Appl. Therm. Eng. 219 (2023) 119626, https://doi.org/10.1016/j.applthermaleng. 2022.119626.

[13] K. Monika, S.P. Datta, Comparative assessment among several channel designs with constant volume for cooling of pouch-type battery module, Energ. Conver. Manage. 251 (2022) 114936, https://doi.org/10.1016/j.enconman.2021.114936.

[14] Y. Huang, P. Mei, Y. Lu, R. Huang, X. Yu, Z. Chen, A.P. Roskilly, A novel approach for Lithium-ion battery thermal management with streamline shape mini channel cooling plates, Appl. Therm. Eng. 157 (2019) 113623, https://doi.org/10.1016/j.applthermaleng. 2019.04.033.

[15] W. Zuo, Y. Zhang, J. E, J. Li, Q. Li, G. Zhang, Performance comparison between single S-channel and double S-channel cold plate for thermal management of a prismatic LiFePO4 battery, Renew. Energy 192 (2022) 46–57, https://doi.org/10.1016/j.renene.2022.04.116.

[16] K. Monika, C. Chakraborty, S. Roy, S. Dinda, S.A. Singh, S.P. Datta, An improved mini-channel based liquid cooling strategy of prismatic LiFePO4 batteries for electric or hybrid vehicles, J. Storage Mater. 35 (2021) 102301, https://doi.org/10.1016/j.est.2021. 102301.

[17] M. Mubashir, J. Xu, Z. Guo, X. Wang, C. Shi, X. Mei, Experimental and numerical investigation of single and double serpentine channel cold plates on the thermal performance of lithium ion pouch battery, J. Storage Mater. 92 (2024) 112200, https://doi.org/10.1016/j.est.2024.112200.

[18] M.S. Patil, J.-H. Seo, S. Panchal, S.-W. Jee, M.-Y. Lee, Investigation on thermal performance of water-cooled Li-ion pouch cell and pack at high discharge rate with U-turn type microchannel cold plate, Int. J. Heat Mass Transf. 155 (2020) 119728, https://doi.org/10.1016/j.ijheatmasstransfer.2020.119728.

[19] W. Qi, P. Lan, J. Yang, Y. Chen, Y. Zhang, G. Wang, F. Peng, J. Hong, Multi-U-Style micro-channel in liquid cooling plate for thermal management of power batteries, Appl. Therm. Eng. 256 (2024) 123984, https://doi.org/10.1016/j.applthermaleng.2024.123984.

[20] F. Liu, Y. Chen, W. Qin, J. Li, Optimal design of liquid cooling structure with bionic leaf vein branch channel for power battery, Appl. Therm. Eng. 218 (2023) 119283, https://doi.org/10.1016/j.applthermaleng.2022.119283.

[21] J.H. Pu, Y. Li, R.C. Li, N. Hua, H. Zhang, Y. Lu, S. Panchal, R. Fraser, M. Fowler, X.-K. Zhang, Design and performance of a compact lightweight hybrid thermal management system using phase change material and liquid cooling with a honeycomb-like structure for prismatic lithium-ion batteries, J. Power Sources 624 (2024) 235632, https://doi.org/10.1016/j. jpowsour.2024.235632.

[22] X.-W. Tian, W. Wang, P. Li, C. Sun, C.-S. Wang, S.-H. Qian, M. Wang, Free-shape modeling and optimization for cold plates with tree-like channels, Int. J. Mech. Sci. 245 (2023) 108076, https://doi.org/10.1016/j.ijmecsci.2022.108076.

[23] S. Zhan, L. Liang, Z. Li, C. Yu, F. Wang, Topology optimization of liquid cooling plate for lithium battery heat dissipation based on a bionic leaf-vein structure, Int. J. Heat Mass Transf. 231 (2024) 125898, https://doi.org/10.1016/j.ijheatmasstransfer. 2024.125898.

[24] R. Yan, Q. Zhao, C. Zhang, Q. Tang, H. Li, Research on liquid-cooling structure for lithium-ion battery with bionic leaf-vein liquid channels, Int. J. Heat Fluid Flow 112 (2025) 109743, https://doi.org/10.1016/j.ijheatfluidflow.2025.109743.

[25] F. Zhang, Z. Huang, S. Li, S. Sun, H. Zhao, Design and thermal performance analysis of a new micro-fin liquid cooling plate based on liquid cooling channel finning and bionic limulus-like fins, Appl. Therm. Eng. 237 (2024) 121597, https://doi.org/10.1016/j. applthermaleng.2023.121597.

[26] Y. Wang, X. Xu, Z. Liu, J. Kong, Q. Zhai, H. Zakaria, Q. Wang, F. Zhou, H. Wei, Optimization of liquid cooling for prismatic battery with novel cold plate based on butterfly-shaped channel, J. Storage Mater. 73 (2023) 109161, https://doi.org/10.1016/j.est.2023.109161.

[27] H. Li, X. Ding, F. Meng, D. Jing, M. Xiong, Optimal design and thermal modelling for liquid-cooled heat sink based on multi-objective topology optimization: an experimental and numerical study, Int. J. Heat Mass Transf. 144 (2019) 118638, https://doi.org/10.1016/j.ijheatmasstransfer. 2019.118638.

[28] F. Chen, J. Wang, X. Yang, Topology optimization design and numerical analysis on cold plates for lithium-ion battery thermal management, Int. J. Heat Mass Transf. 183 (2022) 122087, https://doi.org/10.1016/j.ijheatmasstransfer.2021.122087.

[29] X. Xiang, R. Yang, H. Sun, D. Hoffman, Performance improvement of a hybrid battery thermal management system with pseudo-3D topology optimization, Int. J. Heat Mass Transf. 240 (2025) 126632, https://doi.org/10.1016/j.ijheatmasstransfer.2024.126632.

[30] V. Pandey, P.S. Lee, Maximizing liquid-cooled heat sink efficiency with advanced topology-optimized fin designs, Int. J. Heat Mass Transf. 229 (2024) 125746, https://doi.org/10.1016/j.ijheatmasstransfer.2024.125746.

[31] J. Wu, H. Liu, C. Li, C. Li, G. Xie, Topological optimization and thermal performance of cold plates for lithium-ion battery with non-uniform heat sources, Appl. Therm. Eng. 254 (2024) 123922, https://doi.org/10.1016/j.applthermaleng.2024.123922.

[32] Z. Wang, Z. Zou, Y. Zhou, X. Geng, Y. Sun, X. Huang, M. Hao, Performance comparison of battery cold plates designed using topology optimization across laminar and turbulent flow regime, Int. J. Heat Mass Transf. 238 (2025) 126450, https://doi.org/10.1016/j.ijheatmasstransfer.2024.126450.

[33] K.-H. Cho, C.-W. Choi, Hydraulic-thermal performance of vascularized cooling plates with semi-circular cross-section, Appl. Therm. Eng. 33–34 (2012) 157–166, https://doi.org/10.1016/j. applthermaleng.2011.09.029.

[34] J. E, S. Xu, Y. Deng, H. Zhu, W. Zuo, H. Wang, J. Chen, Q. Peng, Z. Zhang, Investigation on thermal performance and pressure loss of the fluid cold-plate used in thermal management system of the battery pack, Appl. Therm. Eng. 145 (2018) 552–568. doi: 10.1016/j.applthermaleng.2018.09.048.

[35] R. Guo, L. Li, Heat dissipation analysis and optimization of lithium-ion batteries with a novel parallel-spiral serpentine channel liquid cooling plate, Int. J. Heat Mass Transf. 189 (2022) 122706, https://doi.org/10.1016/j.ijheatmasstransfer.2022.122706.

[36] F. Zhang, X. Li, H. Zhao, Z. Huang, X. Lu, Y. Shi, Symmetrical complex serpentine channel introduction of secondary openings with open Y fins integrated optimization design, Int. J. Therm. Sci. 195 (2024) 108620, https://doi.org/10.1016/j.ijthermalsci.2023.108620.

[37] Q. Jiang, Y. Zhang, Y. Liu, R. Xu, J. Zhu, J. Wang, Structural optimization of serpentine channel water-cooled plate for lithium-ion battery modules based on multi-objective Bayesian optimization algorithm, J. Storage Mater. 91 (2024) 112136, https://doi.org/10.1016/j.est.2024.112136.

[38] E.S. Shrinet, R. Akula, L. Kumar, Improvement in serpentine channel based battery thermal management system geometry using variable contact area and its multi-objective design optimization, J. Storage Mater. 96 (2024) 112726, https://doi.org/10.1016/j.est.2024.112726.

[39] X. Pang, Y. Huo, H. Fang, Z. Rao, Analysis of temperature uniformity of electric vehicle battery system with swirling flow strengthened heat transfer, Appl. Therm. Eng. 193 (2021) 116995, https://doi.org/10.1016/j.applthermaleng.2021.116995.

[40] K. Monika, C. Chakraborty, S. Roy, S. Dinda, S.A. Singh, S.P. Datta, Parametric investigation to optimize the thermal management of pouch type lithium-ion batteries with mini-channel cold plates, Int. J. Heat Mass Transf. 164 (2021) 120568, https://doi.org/10.1016/j.ijheatmasstransfer. 2020.120568.

[41] S. Zeng, B. Kanargi, P.S. Lee, Experimental and numerical investigation of a mini channel forced air heat sink designed by topology optimization, Int. J. Heat Mass Transf. 121 (2018) 663–679, https://doi.org/10.1016/j.ijheatmasstransfer.2018.01.039.

[42] H. Ma, L. Su, B. He, D. He, Y. Kang, New design of U-turn type minichannel cold plate with hybrid fins for high temperature uniformity, Int. Commun. Heat Mass Transfer 135 (2022) 106078, https://doi.org/10.1016/j.icheatmasstransfer.2022.106078.

[43] T. Deng, Y. Ran, Y. Yin, X. Chen, P. Liu, Multi-objective optimization design of double-layered reverting cooling plate for lithium-ion batteries, Int. J. Heat Mass

Transf. 143 (2019) 118580, https://doi.org/10.1016/j.ijheatmasstransfer.2019.118580.
[44] J. Wang, X. Liu, F. Liu, Y. Liu, F. Wang, N. Yang, Numerical optimization of the cooling effect of the bionic spider-web channel cold plate on a pouch lithium-ion battery, Case Stud. Therm. Eng. 26 (2021) 101124, https://doi.org/10.1016/j.csite.2021.101124.
[45] S. Feng, S. Shan, C. Lai, J. Chen, X. Li, S. Mori, Multi-objective optimization on thermal performance and energy efficiency for battery module using gradient distributed Tesla cold plate, Energ. Conver. Manage. 308 (2024) 118383, https://doi.org/10.1016/j.enconman.2024.118383.
[46] W. Kong, C. Zhang, Z. Ji, Investigation on the cooling effect of a novel composite channel cold plate for lithium-ion battery, J. Storage Mater. 86 (2024) 111183, https://doi.org/10.1016/j.est.2024.111183.
[47] J. Wang, F. Chen, Z. Shao, L. He, Study of the influence of objective functions on the topology optimization design of battery cold plate, Appl. Therm. Eng. 226 (2023) 120326, https://doi.org/10.1016/j.applthermaleng.2023.120326.
[48] H. Li, X. Ding, D. Jing, M. Xiong, F. Meng, Experimental and numerical investigation of liquid-cooled heat sinks designed by topology optimization, Int. J. Therm. Sci. 146 (2019) 106065, https://doi.org/10.1016/j.ijthermalsci.2019.106065.
[49] L. Wang, H. Zuo, B. Zhang, G. Jia, Effects of the cold plate with airfoil fins on the cooling performance enhancement of the prismatic LiFePO4 battery pack, Energy 296 (2024) 131210, https://doi.org/10.1016/j.energy.2024.131210.